Observed Southern Ocean Cloud Properties and Shortwave Reflection. Part I: Calculation of SW Flux from Observed Cloud Properties*

DANIEL T. MCCOY, DENNIS L. HARTMANN, AND DANIEL P. GROSVENOR

Department of Atmospheric Sciences, University of Washington, Seattle, Washington

(Manuscript received 18 April 2014, in final form 3 September 2014)

ABSTRACT

The sensitivity of the reflection of shortwave radiation over the Southern Ocean to the cloud properties there is estimated using observations from a suite of passive and active satellite instruments in combination with radiative transfer modeling. A composite cloud property observational data description is constructed that consistently incorporates mean cloud liquid water content, ice water content, liquid and ice particle radius information, vertical structure, vertical overlap, and spatial aggregation of cloud water as measured by optical depth versus cloud-top pressure histograms. The observational datasets used are Moderate Resolution Imaging Spectroradiometer (MODIS) effective radius filtered to mitigate solar zenith angle bias, the Multiangle Imaging Spectroradiometer (MISR) cloud-top height–optical depth (CTH–OD) histogram, the liquid water path from the University of Wisconsin dataset, and ice cloud properties from *CloudSat*. This cloud database is used to compute reflected shortwave radiation as a function of month and location over the ocean from 40° to 60°S, which compares well with observations of reflected shortwave radiation. This calculation is then used to test the sensitivity of the seasonal variation of shortwave reflection to the observed seasonal variation of cloud properties. Effective radius decreases during the summer season, which results in an increase in reflected solar radiation of 4–8 W m^{-2} during summer compared to what would be reflected if the effective radius remained constant at its annual-mean value. Summertime increases in low cloud fraction similarly increase the summertime reflection of solar radiation by 9–11 W m^{-2}. In-cloud liquid water path is less in summertime, causing the reflected solar radiation to be 1–4 W m^{-2} less.

1. Introduction

Over the last few decades we have gained unprecedented insight into the role of clouds in Earth's radiation budget because of advances in spaceborne instrumentation. The Southern Ocean region (defined as 40°–60°S), while very important to Earth's radiation budget, is less explored and of special interest because of its pristine environment and extensive cloud cover. Of greatest importance to the albedo are the low-topped and optically thick clouds that are ubiquitous in this region (Haynes et al. 2011) and that have a considerable influence on the reflected solar radiation. Given that the low cloud shortwave feedback is found to be the largest source of intermodel spread in climate sensitivity (Bony et al. 2006) and that a strongly negative and localized optical depth feedback has been diagnosed within multimodel ensemble results from phases 3 and 5 of the Coupled Model Intercomparison Project (CMIP3 and CMIP5) over the Southern Ocean (Zelinka et al. 2012, 2013), it is important to fully utilize remote sensing data to better understand cloud processes in this region. To this end we use the strengths of several spaceborne instruments to better define the structure, phase, and particle size of clouds in this region and their seasonal variations. These datasets are used to construct a database of Southern Ocean cloud properties from which reflected shortwave radiation ($SW^{\uparrow}$) may be calculated. This methodology allows us to separate the contributions to the annual-mean and seasonal variations of cloud reflectivity in the Southern Ocean by different physical properties of the clouds.

We have drawn on many remote sensing datasets in order to construct a database of the cloud properties that are needed by radiative transfer models to calculate the

* Supplemental information related to this paper is available at the Journals Online website: http://dx.doi.org/10.1175/JCLI-D-14-00287.s1.

Corresponding author address: Daniel T. McCoy, Department of Atmospheric Sciences, University of Washington, Box 351640, Seattle, WA 98195-1640.
E-mail: dtmccoy@atmos.uw.edu

DOI: 10.1175/JCLI-D-14-00287.1

monthly reflectivity. The applicability of our cloud property construction is tested through comparisons of our ''reconstructed'' reflectivity to that observed by Clouds and the Earth's Radiant Energy System (CERES). Each remote sensing dataset has its own strengths and weaknesses, and each elucidates a different aspect of the cloud population over the Southern Ocean. The observed seasonal variation of cloud properties sheds light on mechanisms that govern cloud processes and the relative importance of the annual cycle of different cloud properties to the reflection of solar radiation.

2. Remotely sensed cloud properties

a. The multi-instrument approach

Cloud properties show considerable variability in the midlatitudes and determining the influence of these variations on the radiative budget is important. To examine the dependence of albedo on the seasonal cycle of cloud properties, we reconstruct the upwelling shortwave radiation (SW) using plane-parallel radiative transfer in combination with the observations of a suite of cloud properties. These properties are cloud fraction, the liquid and ice water paths of these clouds, the effective radius of the particles that compose the liquid and ice, and the vertical structure and spatial coverage of the clouds.

In the creation of mean monthly clouds from observations, we are presented with two options: using a single instrument that measures these cloud properties simultaneously or using a combination of several different instruments, which each measure individual cloud properties that we may then combine in a consistent way. The Moderate Resolution Imaging Spectroradiometer (MODIS) (Foot 1988; Platnick et al. 2003) produces the most comprehensive single set of retrievals of cloud optical properties, but several elements of the MODIS retrieval methodology make using it in synergy with observations from other instruments an attractive strategy.

The fractional coverage of cloud is of paramount importance to the SW flux calculation over dark ocean surfaces. In the Southern Ocean region, the clouds that impact the SW most significantly are the low cloud (Haynes et al. 2011). Thus, we must choose an observation of cloud fraction that is well suited for very accurately retrieving the coverage of cloud and the distribution of cloud in height and optical thickness.

The International Satellite Cloud Climatology Project (ISCCP), MODIS, and Multiangle Imaging Spectroradiometer (MISR) instruments retrieve cloud fraction as well as height and optical depth but with differing fidelity. The cloud mask agrees between these instruments, but the MODIS cloud-top height–optical depth (CTH–OD) histogram differs greatly from those retrieved by ISCCP and MISR (Marchand et al. 2010). This is because optical depth is not retrieved for pixels on cloud edges by MODIS, thus lowering the zonal-mean cloud fraction within the CTH–OD histogram by 10%–35% in the Southern Ocean relative to ISCCP, MISR and the MODIS cloud mask and raising the average optical depth of the clouds within the histogram. While it would be possible to rescale the MODIS CTH–OD histogram by the cloud mask to bring the total coverage of cloud into agreement with other instruments, the probability density function (PDF) of optical depth within the scaled histogram would be tilted in favor of optically thicker clouds, as shown in Marchand et al. (2010). Consequently, this would lead to $SW^{\uparrow}$ calculated from a rescaled CTH–OD histogram to be too large because the mean optical thickness would be biased high.

Given that MODIS is not suited to retrieval of consistent cloud fraction and optical depth for reconstruction of SW flux, we are left to choose between CTH–OD histograms from ISCCP and MISR. ISCCP is shown to retrieve optically thick cloud fractions similar to MISR and MODIS in the tropics and subtropics but produces a lower optically thick cloud fraction than either instrument in the midlatitudes. This behavior is consistent with the latitudinal dependence of ISCCP cloud fractions as the ISCCP transitions from geostationary to polar-orbiting platforms in the midlatitudes (Evan et al. 2007; Marchand et al. 2010). It may also potentially be due to biases in the ISCCP optical depth retrieval induced by the one-dimensional radiative transfer, assumptions as to cloud phase, or the horizontal resolution (Marchand et al. 2010). Not only is the accurate retrieval of cloud fraction important, but the vertical structure of clouds is important as well. Cloud-top retrievals for low clouds using thermal channels are often confused by inversions in temperature, making the MISR multicamera instrument, which detects low cloud tops at a comparable skill to *Cloud–Aerosol Lidar and Infrared Pathfinder Satellite Observations* (*CALIPSO*) (Wu et al. 2009), an excellent choice for accurately diagnosing low cloud amount and top height. Given these issues we have chosen to use MISR to retrieve cloud fraction, optical depth, and height, particularly because low clouds dominate over the Southern Ocean.

Even if the MODIS CTH–OD histogram could be brought into agreement with the retrievals performed by instruments that do not discard cloud edges, there are still considerable problems with using its retrieved liquid and ice water path. Besides the overall omission of MODIS water path retrievals in edge pixels, the liquid and ice water path are empirically determined based on the cloud optical thickness, cloud-top particle radius, and cloud-top thermodynamic phase (Stein et al. 2011).

In the case of clouds flagged by the thermodynamic phase algorithm as cold topped, the optical thickness will potentially be some combination of liquid and ice water signals which are impossible to separate (Horvath and Davies 2007). This is particularly problematic in the midlatitudes, where synoptic systems and mixed-phase boundary layer clouds occur frequently. To disentangle the liquid and ice water paths, we have utilized the microwave liquid water path, which is relatively insensitive to ice (O'Dell et al. 2008), and the combined lidar–radar-derived ice water path (Mace and Deng 2011), which is highly sensitive to larger ice crystals. [Microwave, radar, and lidar data are not available from MODIS and MISR, so data from the University of Wisconsin (UWISC) climatology and *CloudSat* are used.] The use of these datasets to reconstruct the upwelling shortwave radiation, as opposed to optical depth–derived liquid and ice water paths, is arguably a more rigorous challenge because the technique is completely independent of cloud shortwave reflectance, which is the quantity that we ultimately wish to calculate from the cloud properties. While both radar–lidar and microwave techniques might suffer from systematic errors in their retrievals (Chubb et al. 2013; O'Dell et al. 2008), they are likely the most accurate remote sensing observations available that detail the behavior of cloud liquid and ice in cold-topped and mixed-phase clouds.

In summary, observations from a variety of different instruments that are well suited to the remote sensing challenges of the Southern Ocean have been selected. These observations are combined in a consistent way to form a mean cloud scene. While they will suffer from random errors and systematic biases as all observations do, it is argued that the choice of datasets is more optimal for the problem of interest. While using a single instrument to consistently describe the cloud properties in the Southern Ocean has some advantages, in this case the problem of interest and the remote sensing challenges of the region favor a multi-instrument approach. In the following sections, we describe the data from which we will calculate the upwelling SW.

b. Cloud fraction

To measure the cloud fraction we use the MISR CTH–OD histogram (Marchand et al. 2010). Because MISR is a passive instrument, it only detects the height of the topmost cloud layer. Information of cloud coverage beneath visible cloud is not retrieved. To determine the total fraction of cloud coverage in each layer, we combine MISR with cloud overlap information. This may be either a simple assumption such as random overlap or may be inferred from observations such as the *CloudSat* level 2B geometric profile product (2B-GEOPROF; Mace et al. 2009). In the following section, we examine the application of overlap information to the MISR histogram in the creation of an approximate total cloud fraction in several vertical categories.

Overlap probabilities are calculated using the cloud profiling radar (CPR) cloud mask in the 2B-GEOPROF data. In this study we consider clouds segregated based on cloud-top pressure (CTP) into low (CTP $>$ 680 hPa), middle (440 hPa $<$ CTP $<$ 680 hPa), and high (CTP $<$ 440 hPa) categories, consistent with ISCCP definitions of these categories. Throughout the rest of this study, we use the same definitions of the low, middle, and high cloud categories. Because of the simplicity of our three category system, we may explicitly write down the potential overlap cases that we consider in terms of underlying layers and topmost cloudy layer (denoted by a subscript T): $P(L \mid M_T)$ (the probability of a low cloud occurring when a middle-topped cloud is present), $P(L \neg M \mid H_T)$ (the conditional probability of a low cloud beneath a high-topped cloud with no middle cloud), $P(L \wedge M \mid H_T)$ (the conditional probability of a low cloud and a middle cloud when a high cloud is present), and $P(M \mid H_T)$ (the probability of a middle cloud beneath a high cloud). The oceanic zonally averaged daytime only values of these probabilities are shown in Fig. 1. For comparative purposes, we also show the raw cloud fraction detected by *CloudSat* (fractional detection in each cloud category whether or not there is overlying or underlying cloud and analogous to a GCM cloud fraction), written as $P(L)$, $P(M)$, and $P(H)$, and the fractional detection of cloud tops in each category (with no overlying cloud by the CPR and analogous to the cloud fraction a passive instrument would detect), written as $P(L_T)$, $P(M_T)$, and $P(H_T)$. The probability of detecting a low cloud may be written as $P(L) = P(L_T) + P(L \neg M \mid H_T)P(H_T) + P(L \wedge M \mid H_T)P(H_T) + P(L \mid M_T)P(M_T)$, and the probability of detecting a middle cloud may be written as $P(M) = P(M_T) + P(M \mid H_T)P(H_T)$. The total cloud detected may also be compared to the MODIS cloud mask overlapping with the *CloudSat* swath that is contained in the 2B-GEOPROF dataset, as shown in Fig. 2. Uncertainty is estimated for the 2B-GEOPROF cloud fraction by calculating the cloud fraction, including very weak echoes where the reflectivity strength is less than the single-column sensitivity of the radar (Mace 2007). Uncertainty in the MODIS cloud mask overlapping with the 2B-GEOPROF data is calculated using the MODIS cloud mask confidence flag. Given that 2B-GEOPROF does not efficiently detect low, liquid clouds (Stephens et al. 2002), we would not expect it to give a reasonable value for the low cloud overlap cases. This is borne out by the relatively low values of $P(L_T)$ and $P(L)$ as shown in Fig. 1 compared to passive

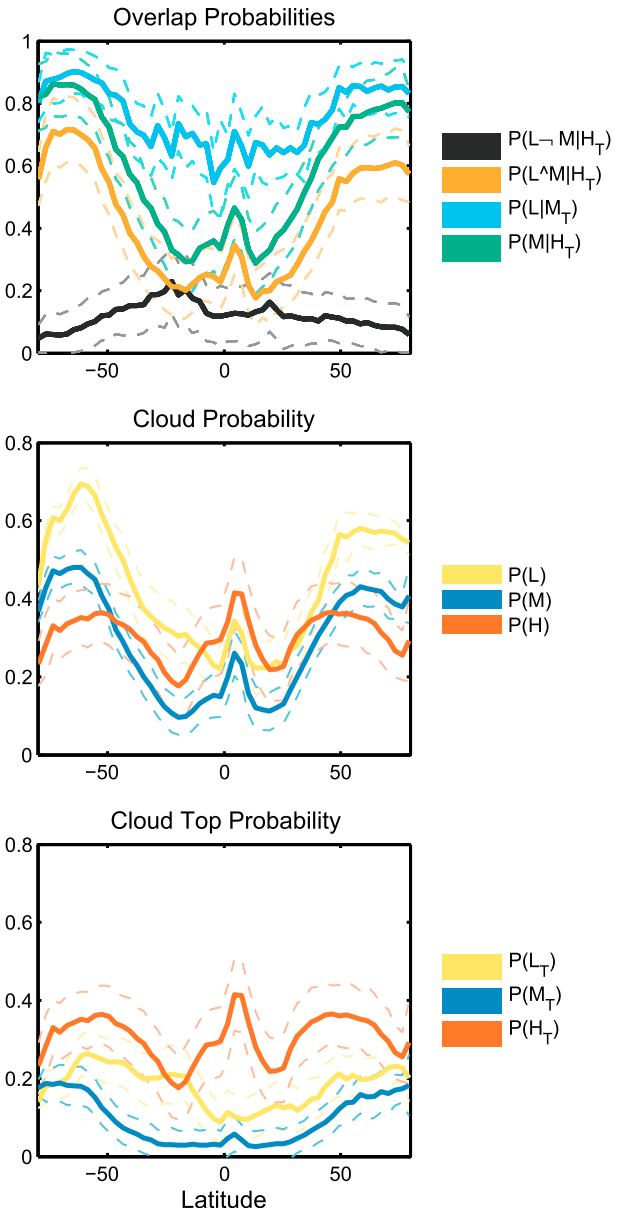

FIG. 1. Probabilities of (top) overlap, (middle) cloud detections, and (bottom) cloud-top detections from 2B-GEOPROF. Error bars are shown with dashed lines. The variables $P(L_T)$, $P(M_T)$, and $P(H_T)$ refer to the fractional occurrence of cloud tops in each category with no overlying cloud. The variables $P(L)$, $P(M)$, and $P(H)$ refer to the total fractional detection of clouds in each height category by the CPR, regardless of other cloud category detections. The variable $P(L \neg M \mid H_T)$ refers to the conditional probability of low cloud and no middle cloud beneath a high cloud, $P(L \wedge M \mid H_T)$ refers to the conditional probability of low cloud and middle cloud when high clouds are present, $P(L \mid M_T)$ gives the conditional probability of a low cloud occurring beneath a middle cloud, and $P(M \mid H_T)$ gives the conditional probability of detecting a middle cloud beneath a high cloud. For further details, refer to the text.

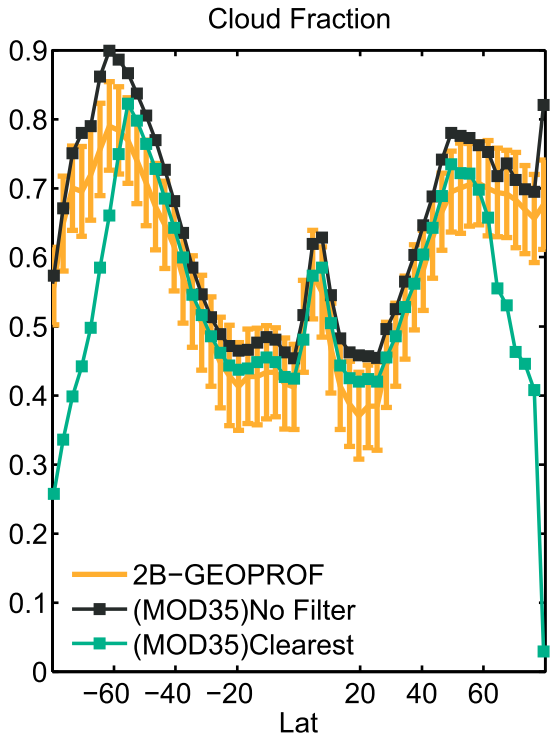

FIG. 2. Total cloud fraction from the MODIS cloud mask (MOD35) compared to the 2B-GEOPROF total cloud coverage. 2B-GEOPROF total cloud fraction is shown in orange. Error bars on 2B-GEOPROF are calculated by inclusion of weak echoes in the CPR cloud mask. MOD35 values are taken from collocated MODIS data along the *CloudSat* track. Data designated as "no filter" ignore the confidence flag assigned to each collocated MODIS retrieval. Data designated as "clearest" assign a cloud fraction of zero to all collocated MODIS data not flagged as a confident retrieval. Data are from the period 2007–08 and are shown over oceans.

estimates as well as the overall lower cloud coverage compared to MODIS cloud mask shown in Fig. 2. On examination of Fig. 1, it is clear that in the Southern Ocean region low and middle clouds are frequently found beneath high clouds.

To examine the seasonal cycle of cloud fraction, we use the native resolution of the MISR histogram at 1° × 1° and interpolate the climatological zonal-mean overlap probabilities from 2B-GEOPROF to this grid. This probability climatology is used to create an approximate overlapped cloud fraction using the MISR CTH–OD histogram for the period 2000–09, as shown in Fig. 3. It should be noted that at latitudes poleward of 50°S during winter high solar zenith angles do not allow MISR to retrieve cloud fraction, and these months have been left blank.

The 40°–60°S region has large fractional coverage of low cloud with a peak amount in the summer (Fig. 3a). Middle cloud fraction peaks in wintertime at 40°S and in

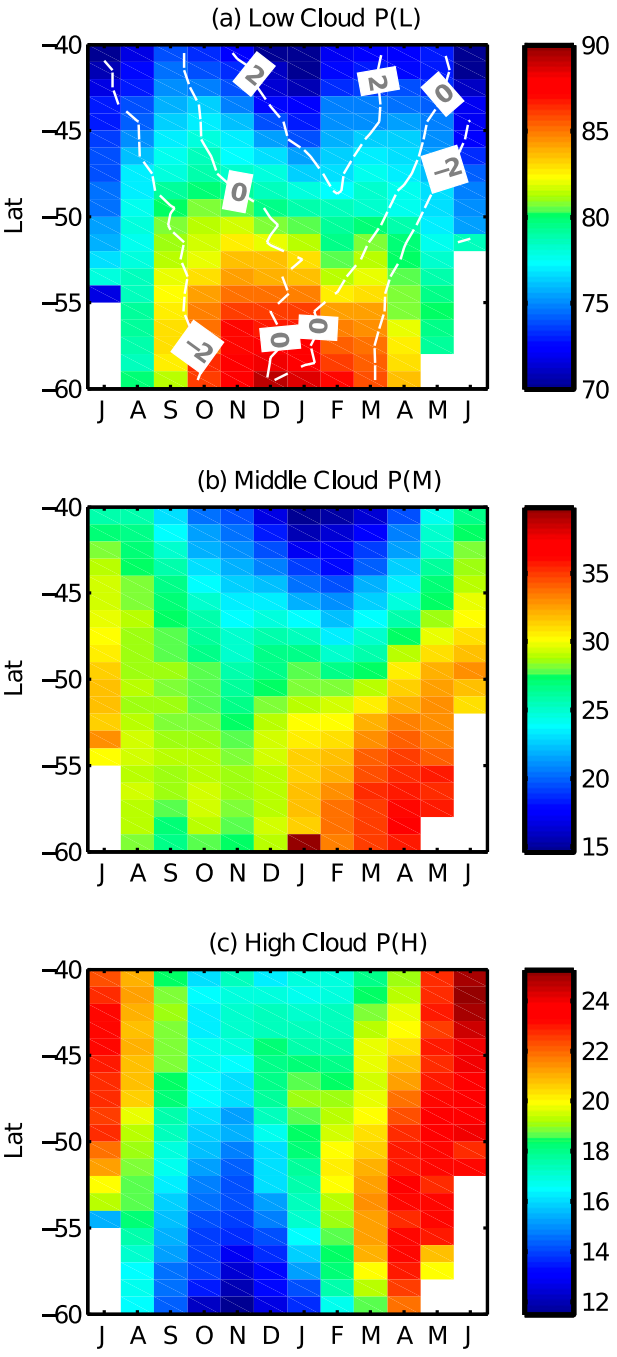

FIG. 3. Cloud fraction (%) in each pressure category for (a) low, (b) middle and (c) high cloud calculated using the MISR CTH–OD histogram combined with overlap data from 2B-GEOPROF [white contours in (a) show random overlap cloud fraction minus 2B-GEOPROF overlap calculated cloud fraction].

summer at 60°S (Fig. 3b). MISR detects a relatively small amount of high cloud, which peaks in the wintertime (Fig. 3c).

Upper-level cloud fraction is underestimated by MISR (Marchand et al. 2007). MISR fails to see tenuous upper-level cloud because height retrieval is dependent on feature contrast. Thus, optically thin cloud above optically thick cloud is typically classified as the optically thick cloud's category because its feature contrast is frequently higher. This leads to optically thin middle and high cloud fraction being underestimated by MISR. Given that our primary interest is to estimate the impact of the radiatively dominant low cloud fraction on the upwelling shortwave radiation (Haynes et al. 2011), we accept this as a known bias.

COMPARISON TO OTHER CLOUD FRACTION RETRIEVALS

The fractional coverage of cloud plays a central role in the calculation of upward radiative flux but presents a variety of remote sensing challenges. Thus, we compare several datasets: our MISR- and 2B-GEOPROF-derived overlapped cloud fraction; the combined *CALIPSO–CloudSat* climatology of cloud fraction of Kay and Gettelman (2009) (for the period 2006–11); the MISR CTH–OD overlapped cloud fraction using a simple random overlap; and the GCM-Oriented *CALIPSO* Cloud Product (*CALIPSO*-GOCCP; Chepfer et al. 2009) (for the period 2006–09). These datasets are shown in Fig. 4. The cloud fraction is split into the 40°–50°S and the 50°–60°S regions. In the more poleward latitude band MISR does not provide retrievals during the winter period of darkness and low sun angle, and thus we must infer the seasonal cycle during this period. The cloud fraction seems to have a similar behavior to the more equatorward region shown in Fig. 4. We can see that in both regions MISR detects distinct seasonal cycles in each cloud category. We find wintertime peaks for middle and high cloud as calculated by the overlap from 2B-GEOPROF that are consistent with previous studies, which diagnosed an upper-level cloud fraction peak in winter driven by extratropical cyclone activity in the Southern Ocean equatorward of 60°S (Bromwich et al. 2012; Haynes et al. 2011). This is also echoed by the seasonal cycle shown by the *CALIPSO–CloudSat* synergy, which is highly suited for the detection of icy upper-level cloud. The season of peak high and midlevel cloud amount differs between the two instruments by a few months, but this may be due to the interplay between solar zenith angle and optical depth. Visible optical depth tends to be overestimated at times of high solar zenith angle (Grosvenor and Wood 2014; Loeb and Coakley 1998; Loeb and Davies 1997; Loeb et al. 1997; Loeb and Davies 1996), which would tend to bias MISR tenuous upper-level cloud detections toward the time of highest solar zenith angle. Finally, the mean amount of middle and high cloud detected by the active instruments is higher in most cases than that diagnosed by MISR, which is consistent with the known

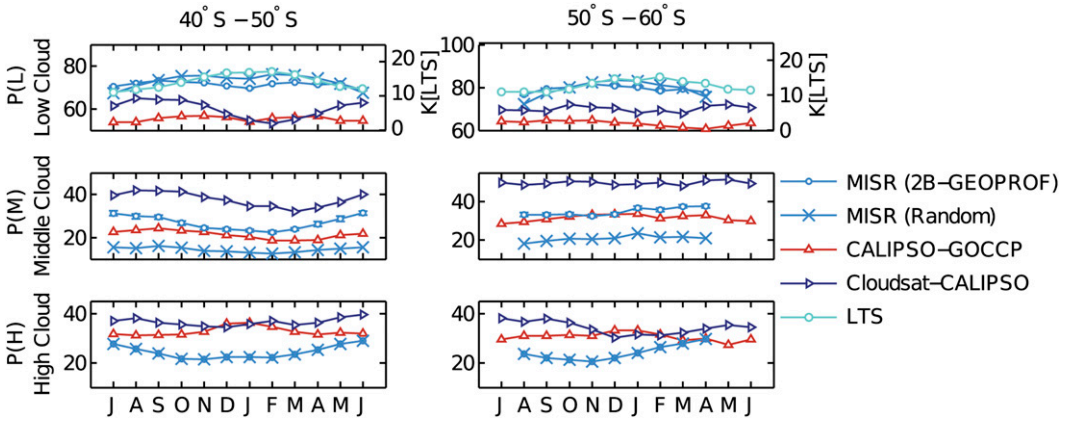

FIG. 4. Intercomparison of cloud fraction from MISR, *CALIPSO–CloudSat*, and GOCCP and the LTS. The seasonal cycles of (top) $P(L)$, (middle) $P(M)$, and (bottom) $P(H)$ are shown. Cloud fraction calculated from MISR is shown using a random overlap assumption and using the correlation found by 2B-GEOPROF. We have separated the plot into two latitude bands. MISR does not retrieve cloud fraction during high-latitude winter and consequently is left blank in the higher-latitude band. The LTS links to the right axis of the low cloud plots and is given in kelvin.

underestimation of tenuous upper-level cloud by the MISR instrument, *CloudSat*'s sensitivity to strongly scattering ice particles, and *CALIPSO*'s sensitivity to optically thin cirrus.

Comparison between low-level cloud fraction as inferred by MISR assuming a random overlap shows qualitatively the same cycle as the 2B-GEOPROF overlap combined with MISR with slight underestimation during the winter and overestimation during the summer, which is consistent with attenuation by thick cloud and underdetection of liquid cloud. The overall amount peaks in summer, which is consistent with the cloud fraction being stability dependent (Klein and Hartmann 1993; Wood and Bretherton 2006) and going in step with lower-tropospheric stability (LTS) (Slingo 1980). The LTS calculated from the European Centre for Medium-Range Weather Forecasts (ECMWF) Interim Re-Analysis (ERA-Interim) is consistent with this notion, showing peak inversion strength during warmer months in step with low cloud fraction (Fig. 4).

While the differences in overlap scheme may not have as great a qualitative effect on low cloud, we argue that random overlap is not appropriate for diagnosing middle cloud. Both the synoptic activity peak in winter in the Southern Ocean and the measured cloud fraction from *CALIPSO–CloudSat* support the notion of a wintertime peak in middle and high cloud, which requires correlation between middle and high cloud. Thus, we utilize the measured probability of overlap from 2B-GEOPROF to diagnose middle cloud beneath high cloud. This seems especially apt given that both middle and high cloud are reflective to radar because they are primarily ice phase. The correlation between middle and high cloud occurrence is expected if they are both driven by storm-track activity.

Another source of disagreement between the *CALIPSO–CloudSat* and MISR+2B-GEOPROF data is in the seasonal cycle of low cloud, which MISR shows as peaking in the warmer months and at generally higher fractional coverage than *CALIPSO–CloudSat* (Fig. 4), while *CALIPSO–CloudSat* shows a rough wintertime peak with less low cloud. This disagreement is consistent with the nature of *CALIPSO–CloudSat* and MISR, the former is highly accurate at detecting upper-level clouds and the latter at optically thick clouds. *CloudSat* misses a large amount of optically thin liquid cloud and *CALIPSO–CloudSat* excludes the bottom 720 m (Stephens et al. 2002; Kay and Gettelman 2009). Globally, *CloudSat* is estimated to detect only 70% of all liquid cloud over oceans (Stephens et al. 2002). The increase in wintertime in-cloud ice water path (IWP; shown in Fig. 8a) leads us to hypothesize that the wintertime peak in low cloud, as diagnosed by active remote sensing, is more a result of an increase in radar reflectivity than an overall increase in low cloud coverage.

Finally, comparison with GOCCP, which is able to detect a larger fraction of liquid clouds than *CloudSat*, although it suffers heavily from attenuation, shows a similar cycle in low cloud in the 40°–50°S band to MISR, leading us to believe that this cycle is real and not an artifact of MISR's cloud detection algorithm. It is unclear if the difference between these two low cloud retrievals in the more poleward region from 50° to 60°S is due to increased attenuation of the lidar by thick upper-level cloud or if the MISR histogram is in error. Given the consistency of the MISR histogram and the simplicity of the method by which we retrieve the low cloud fraction from the observed cloud tops, we believe the MISR low cloud in this region is physically reasonable.

c. Liquid water path

We calculate an approximate in-cloud liquid water path using a combination of several instruments over the period 2001–08. To calculate the upwelling SW and determine the contributions due to variability of liquid water content in different cloud categories, we must know not only the amount but also the vertical distribution of liquid water. Microwave and optical techniques are able to retrieve liquid water path, but both retrieve integrated quantities that are not vertically resolved and the latter cannot distinguish between signals originating from ice and liquid (Horvath and Davies 2007). The liquid water content calculated from millimeter wave radar reflectivity contained in the *CloudSat* level 2B radar-only cloud water content product (2B-CWC-RO; Austin and Stephens 2001) retrieves a vertically or horizontally resolved profile of liquid content but is limited by the inability of radar to determine thermodynamic phase in the mixed-phase cloud and thus the necessity of assuming phase attribution in the mixed-phase temperature range (Huang et al. 2012). To reduce biases in the vertically resolved liquid water content introduced by these limitations, we force the integrated liquid water path to be consistent with the passive microwave liquid water path in the UWISC dataset, which is well attuned to the detection of liquid (O'Dell et al. 2008). This is done by calculating the ratio of liquid water in each pressure category to the vertically integrated liquid water path as determined by the 2B-CWC-RO algorithm, which uses the reflectivity measured by *CloudSat* in combination with the temperature profile. The zonal-mean behavior of this ratio is shown in Fig. 5, and uncertainty in this quantity is calculated using the uncertainty in the 2B-CWC-RO data. This ratio may then be used to partition the vertically integrated daytime liquid water path measured using passive microwave. The UWISC liquid water data has been chosen over optical depth based methods because it produces a low systematic error in the Southern Ocean and is able to retrieve liquid water effectively in clouds that contain both ice and liquid (O'Dell et al. 2008). The daytime liquid water path is calculated from the diurnal cycle provided in the UWISC dataset. This method provides a liquid water path in three layers (consistent with the low, middle, and high pressure categories) that we then divide by the overlapped MISR cloud fraction from the preceding section to yield an in-cloud liquid water path in each pressure category. Creation of a vertically resolved liquid water path by this method offers improvement on simply assuming a vertical partitioning of liquid amount based on the temperature profile. This technique indicates that most of the liquid water is in the low clouds in the midlatitudes, as shown in Fig. 5.

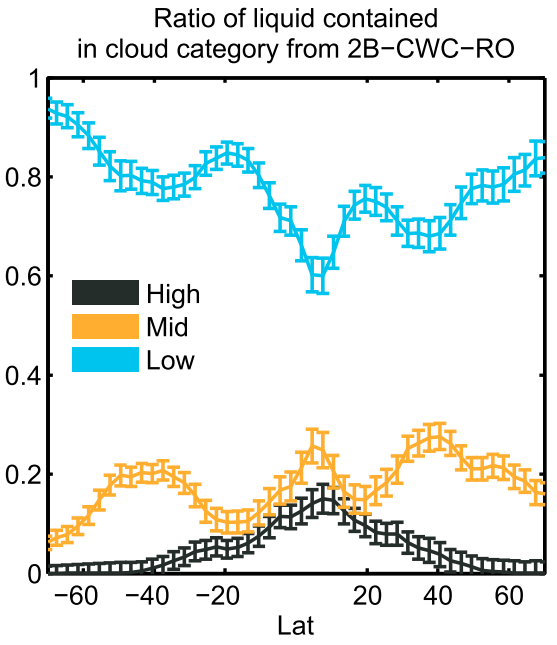

FIG. 5. The annual-mean fraction of column LWP contained in low, middle, and high categories as calculated by the 2B-CWC-RO algorithm. Error bars are propagated from uncertainty in the 2B-CWC-RO.

The middle and high in-cloud liquid content generated by this technique is found to change with temperature (Figs. 6b,c). Both middle and high in-cloud liquid water path are maximum in summertime with a general trend toward higher in-cloud liquid content at lower latitudes (warmer temperatures). While it should be noted that the in-cloud upper-level liquid water path is quite large, this is an effect of MISR detecting too little high cloud cover and thus biasing in-cloud liquid water in this pressure regime. When averaged horizontally over the entire scene, the amount of liquid water at pressures below 440 hPa is negligible and so does not significantly impact the calculation of $SW^{\uparrow}$. Both *CloudSat*-derived overlap for low cloud and random overlap show an increase in low cloud liquid water path in the fall and wintertime (Fig. 6a).

d. Ice water path

Because of the large particle size of ice, lidar and radar data from both *CALIPSO* and *CloudSat* are sensitive to ice and combined information from these instruments is used to constrain the level 2C ice cloud property retrieval product (2C-ICE; Mace and Deng 2011). When used in conjunction, these instruments allow the creation of a vertical profile of ice water content and ice particle effective radius that contains both the tenuous ice clouds detected by lidar and the optically thicker clouds to which radar is sensitive. Validation of this product in the Tropical Composition, Cloud, and Climate Coupling (TC4)

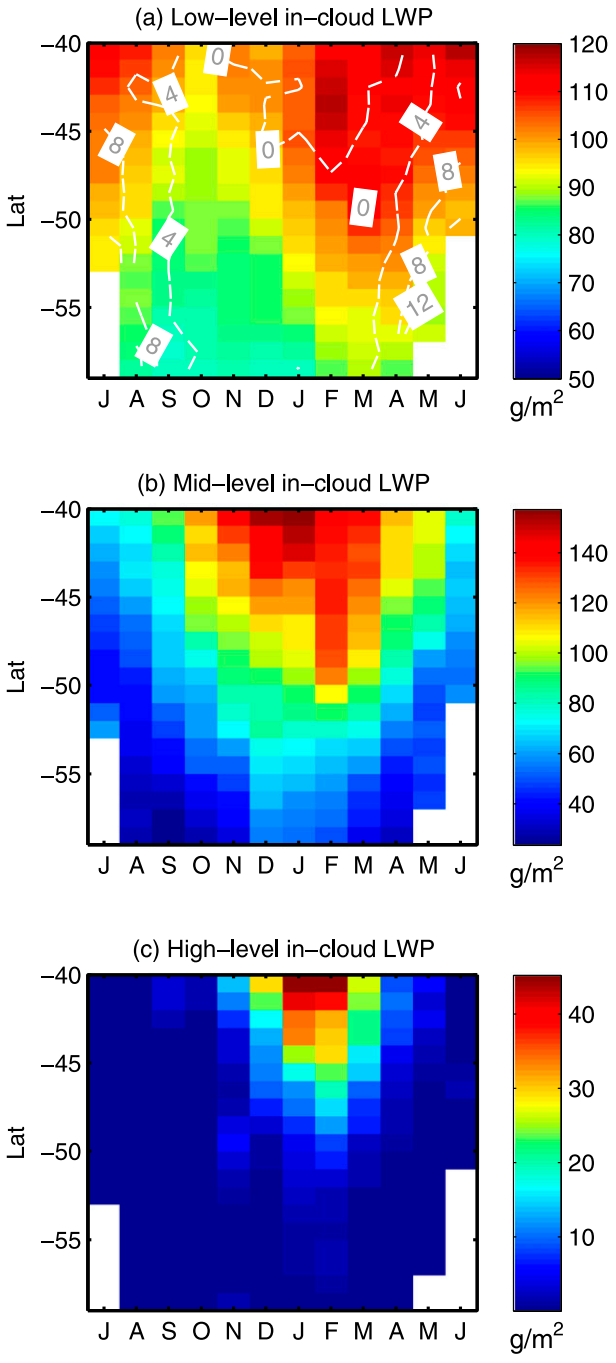

FIG. 6. In-cloud LWP for (a) low, (b) middle, and (c) high level calculated using overlapped MISR cloud fraction and approximate vertical LWP from combined UWISC LWP and *CloudSat* vertical liquid content. Differences between the random overlap and 2B-GEOPROF overlap calculated in-cloud LWP are shown for low cloud with white contours in (a). In most regions the differences are minimal, with the largest difference existing in winter.

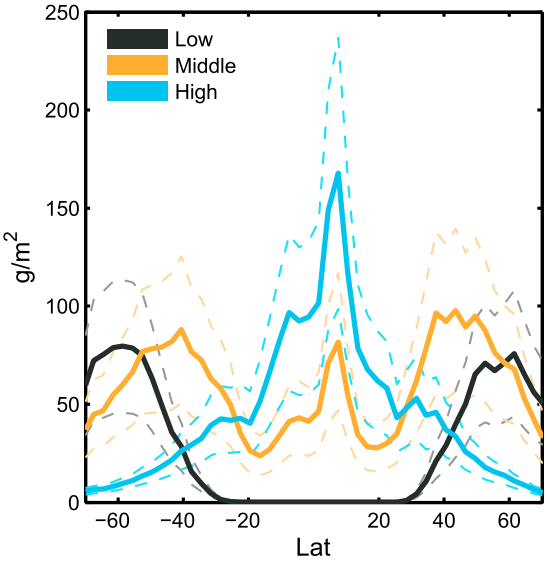

FIG. 7. IWP from 2C-ICE in each height category, shown over oceans and from the period 2007–08. Error bars are shown as dashed lines and are given by the mean uncertainty specified in the 2C-ICE dataset.

and Small Particles in Cirrus (SPARTICUS) field campaigns has shown good agreement between the ice effective radius r_{ge} and IWC retrieved by the 2C-ICE algorithm and the in situ measurements of these quantities (Deng et al. 2010; Heymsfield et al. 2008), although its retrievals of boundary layer ice clouds may tend to be biased high in the Southern Ocean because of attributing reflections from large cloud droplets to ice crystals (Chubb et al. 2013). The integrated IWP in each category is shown in Fig. 7.

We use data from the period 2007–08 from the 2C-ICE product, divided by the cloud fraction from MISR in each level, to give an in-cloud ice water path over the Southern Ocean. Low-altitude in-cloud ice water path is found to increase strongly in winter; high-altitude in-cloud IWP shows a summertime peak; and middle-altitude in-cloud IWP shows a wintertime peak at low latitudes, which transitions to a summertime peak at higher latitudes (Fig. 8). We have removed points whose ice water is in excess of $4\,\mathrm{kg\,m^{-2}}$ from the mean, which are assumed to be artifacts of underdetection by MISR of optically thin ice clouds over high contrast boundary layer cloud. These data points account for less than 0.0001% of the total volume of data. In addition, during September 2008, insufficient swaths were available in the *CloudSat* data archive at the time of writing to achieve good coverage and the September data from 2007 was substituted in its place.

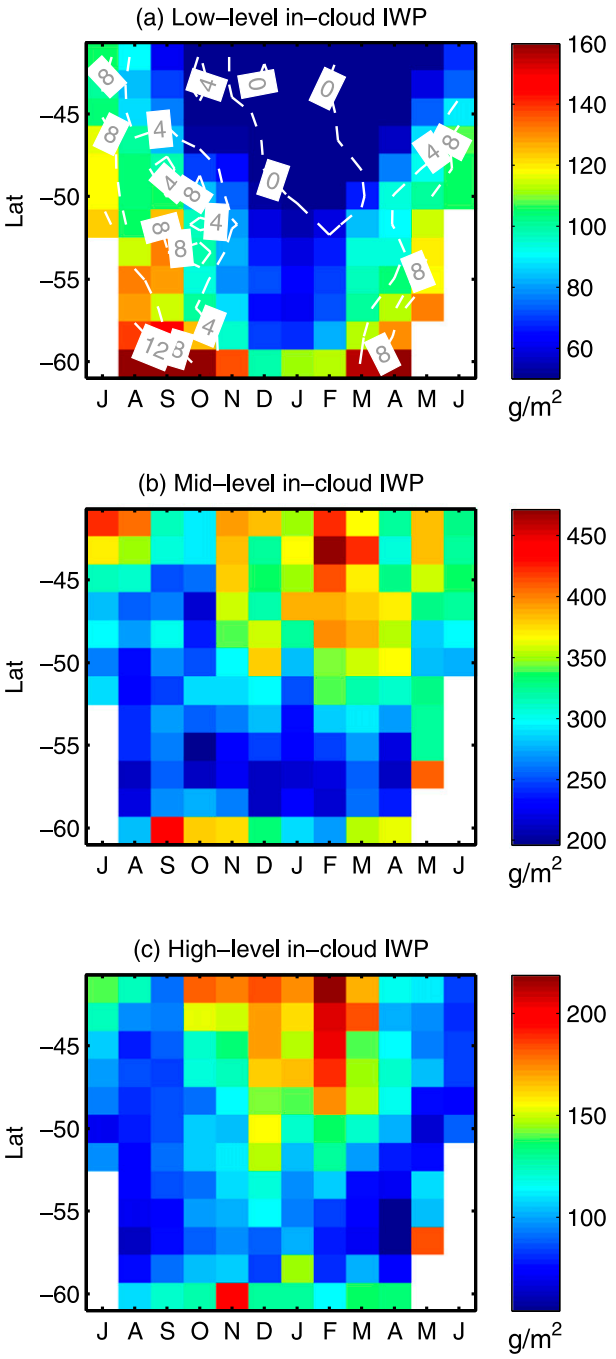

FIG. 8. In-cloud IWP for (a) low, (b) middle, and (c) high level calculated using overlapped MISR cloud fraction and 2C-ICE IWP. Differences between the random overlap and 2B-GEOPROF overlap calculated in-cloud LWP are shown for low cloud with white contours in (a). In most regions the differences are minimal, with the largest difference existing in winter.

The creation of an in-cloud ice water path by this method tends to bias the value toward being too high in upper-level cloud because tenuous ice clouds are frequently undetected by MISR and may be biased slightly high by 2C-ICE (Deng et al. 2010). We use this technique to be consistent with our calculation of in-cloud liquid in the preceding section. While our method tends to fail when dealing with upper-level cloud, we choose data and methods with the intent of resolving the low cloud as accurately as possible because low cloud is the primary contributor to the cloud radiative effect in this region (Haynes et al. 2011). The seasonal cycle of in-cloud IWP at pressures above 680 hPa seems relatively strong and physically plausible. Together, the liquid and ice water paths show an increase in low cloud total water path during the winter. This may be caused by efficient longwave cooling at cloud top during the high-latitude winter darkness, leading to buoyant production of turbulence and an increase in liquid, where some of which transitions to ice (Curry 1986; Morrison et al. 2011; Solomon et al. 2011), as well as more active dynamics during the winter season (Simmonds et al. 2003; Verlinden et al. 2011).

The effective radius of ice diagnosed by 2C-ICE in the Southern Ocean differs between cloud categories, with low, middle and high clouds having a mean effective radius and RMS uncertainty of 61 ± 6, 50 ± 5, and 35 ± 5 μm, respectively. Middle and high clouds have somewhat higher values in the summer, but the difference is smaller than the RMS uncertainty attached to the dataset.

e. *Liquid effective radius*

The MODIS instruments onboard the *Aqua* and *Terra* polar-orbiting satellites retrieve liquid cloud effective radius r_e based upon the combination of one non-absorbing optical wavelength and one absorbing near-infrared band (Foot 1988; Nakajima and King 1990; King et al. 1997; Platnick et al. 2003). The latter can be 1.6, 2.1, or 3.7 μm, although prior to the upcoming collection 6 only the 2.1-μm band is available for level-3 products. Retrieving r_e remotely is somewhat uncertain and yet very important because the reflectivity of clouds is sensitive to r_e in the size range of typical marine stratocumulus droplets. King et al. (2013), Breon and Doutriaux-Boucher (2005), and Painemal and Zuidema (2011) have diagnosed overestimation of r_e in marine stratocumulus by the standard retrieval approach relative to in situ measurements and the Polarization and Directionality of the Earth's Reflectances (POLDER).

Furthermore, large differences between r_e from these different bands have been observed (Zhang and Platnick 2011; Zhang et al. 2012), although the magnitude of these differences varies and is generally fairly small in high cloud fraction stratocumulus regions (Zhang and Platnick 2011; Zhang et al. 2012; Painemal and Zuidema 2011; King et al. 2013). Such spectral differences generally become larger in more strongly precipitating regions and it

has been suggested that this reflects vertical changes in r_e as a result of the presence of precipitation hydrometeors (Chen et al. 2008) and the differing penetration depths of the three bands (Platnick 2000). However, recent evidence has suggested that precipitation hydrometeors would have little effect on the retrieved r_e (Zhang et al. 2012; Zinner et al. 2010) and that the MODIS instrument information content may not be sufficient to discriminate vertical variations in r_e (King and Vaughan 2012). Precipitating regions are also associated with increased cloud heterogeneity and recent evidence suggests that this is a major cause of r_e differences between the different bands (Zhang et al. 2012; Painemal et al. 2013). Additionally, Zhang (2013) showed that the wide droplet size distributions present in precipitating regions can lead to spectral differences. The prevalence of drizzling low cloud in the Southern Ocean (Haynes et al. 2011) increases the likelihood of such retrieval problems for this region.

Based upon observations of Arctic stratocumulus Grosvenor and Wood (2014) showed that the solar zenith angle θ_0 at which MODIS retrievals are made will likely affect r_e. Reductions in the mean r_e of up to 9% relative to low θ_0 retrievals were observed for $\theta_0 > 65°$, depending upon view zenith angle and wavelength. Solar zenith angle was also shown to affect the relative differences in mean r_e between the different bands; at low θ_0 there was very little relative difference, whereas at high θ_0 a spread of around 1 μm was observed. As in other studies, the sign and magnitude of these relative differences was found to be dependent on the cloud heterogeneity. Given all of the above, it is useful to consider r_e data retrieved from the different bands as this may give some estimate of the degree of uncertainty in MODIS r_e.

Because of the inconsistencies in the MODIS retrieval at high θ_0, in order to obtain a consistent r_e dataset it is prudent to restrict MODIS retrievals to $\theta_0 < 65°$. A global dataset akin to MODIS level 3 with such a restriction has been assembled from one year of MODIS collection 5.1 level-2 data from the *Terra* and *Aqua* satellites, as described in Grosvenor and Wood (2014). This dataset also contains r_e retrievals from the different r_e bands. Further, only data from $1° \times 1°$ grid boxes for which the liquid cloud fraction is >80% are included in an attempt to avoid r_e biases due to cloud heterogeneity within broken cloud scenes (e.g., see Wood and Hartmann 2006; Bennartz 2007). Comparison to the standard collection 5.1, level-3 product, which is based on the 2.1-μm channel (Fig. 9), shows that the new dataset r_e values are around 1 μm lower, despite the removal of high θ_0 retrievals that were likely biased low. This is due to the effect of the >80% cloud fraction screening. As observed in the previous studies mentioned above, large

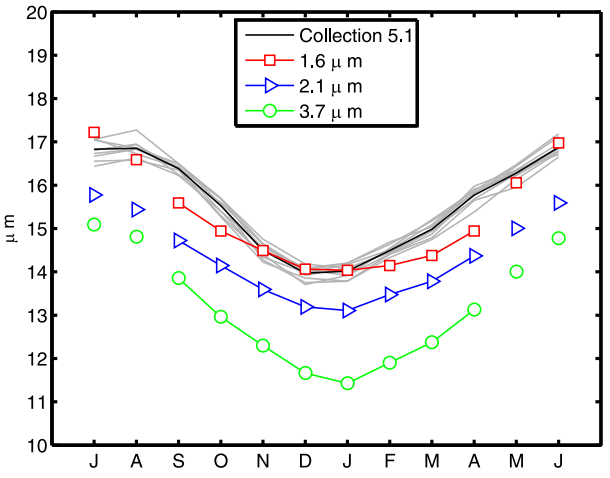

FIG. 9. Comparison of the average annual cycle from the MODIS collection 5.1 r_e to the 1.6-, 2.1-, and 3.7-μm channel r_e retrievals as calculated using the methodology of Grosvenor and Wood (2014). Gray lines are individual annual cycles from 2002 to 2011 from the collection 5.1 data, and the solid black line is a mean over these years. Because of the constraint on θ_0, data during the wintertime must be interpolated. Interpolated values are shown using only a symbol.

differences between the different MODIS bands of up to almost 3 μm are apparent in the monthly means. Here we take these differences as being representative of retrieval uncertainties.

Each r_e retrieval shows a consistent decrease in summer and an increase in winter (Fig. 10). The collection 5.1 results show that the annual cycle of r_e is fairly robust from year to year, leading us to believe that the single year of data from our modified dataset is a relatively good representation of the long-term climatology. However, since the collection 5.1 dataset contains retrievals at very high θ_0 during wintertime, it is possible that some of this cycle is an artifact of θ_0 on the retrieval of r_e. Such high θ_0 retrievals have been removed from the modified dataset, but as a result it has data missing in the wintertime when θ_0 is always >65°. Given that the collection 5.1 dataset shows a relatively smooth behavior in winter, we use a spline interpolation to fill in the missing wintertime data in the modified dataset. Grosvenor and Wood (2014) showed that retrievals of r_e at high θ_0 (as occur in winter) are likely to be biased low compared to retrievals at low θ_0. Therefore, the amplitude of the annual cycle from collection 5.1 is likely to be underestimated compared to the real cycle and thus can be taken as a lower limit of seasonal variation. It should be noted that it is unknown whether the absolute values of r_e in the new dataset are correct. However, the variation of r_e through the seasonal cycle is likely to be less prone to seasonally dependent biases (e.g., resulting from θ_0) and to heterogeneity biases, which may also

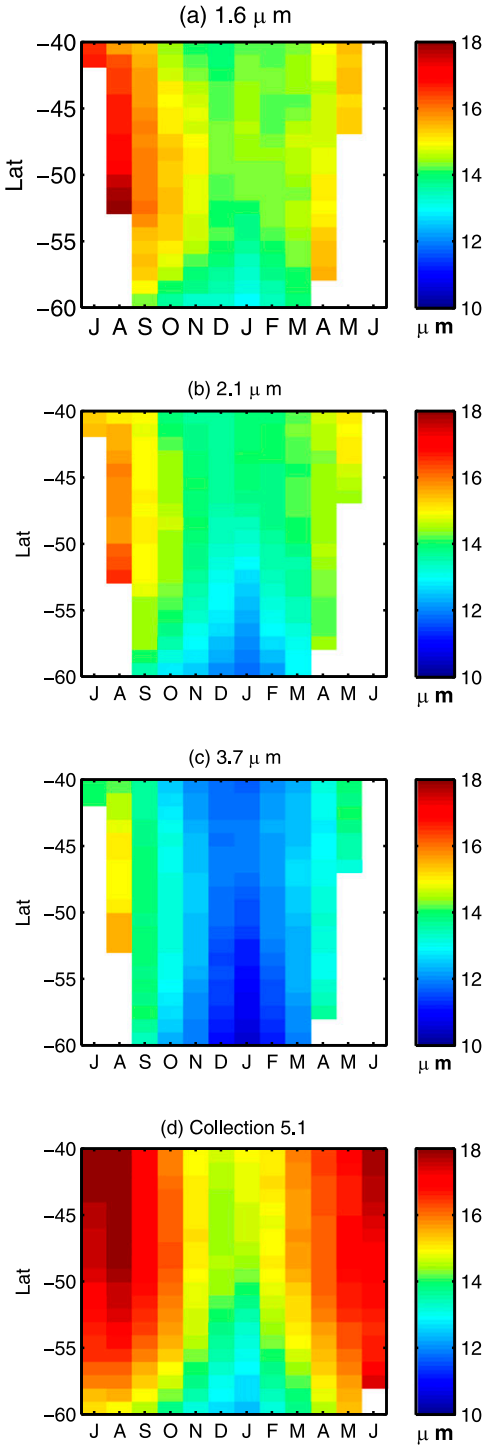

FIG. 10. The r_e from MODIS in the Southern Ocean region from 40° to 60°S. The r_e is retrieved from (a)–(c) individual channels (as described in the text) and (d) the collection 5.1 product.

vary seasonally, and thus the amplitude of the cycle is likely to be more accurate.

It is possible that the seasonal r_e cycle is simply due to the meteorology of the clouds in this region leading to changing cloud-top liquid water contents (LWCs). On the other hand, for a constant LWC, it is also consistent with an increase in the cloud-top droplet number concentration N_d and therefore the notion of the peaking of ocean biogenic production of cloud condensation nuclei (CCN) in summer (Korhonen et al. 2008; Vallina et al. 2006). Calculations of N_d (not shown) using the method of Bennartz (2007) show a seasonal cycle that is consistent with this. The N_d calculation takes into account any changes in cloud LWP, suggesting that seasonal LWC and meteorological variability are not the cause of the r_e cycle. It is unlikely that the seasonal cycle of effective radius is driven by sea salt emissions because they are found to only vary weakly and to be at maximum in winter, rather than in summer (Vallina et al. 2006). Further, for a cloud in which the liquid water content increases adiabatically and for which N_d is constant in the vertical $r_e \propto \mathrm{LWP}^{1/6} N_d^{-1/3}$. Given this, it is likely that r_e is twice as sensitive to changes in N_d than to changes in LWP, indicating that seasonal changes in N_d are likely to play a significant role in the observed seasonal variation of r_e.

3. The creation of a cloud database and the calculation of $SW^{\uparrow}$

In this section, we will describe the process by which we create a database of cloud properties that is consistent with observations and from which the upwelling SW may be calculated utilizing plane-parallel radiative transfer. In the creation of this database, our objective is to bring the observations of the distribution of clouds in optical depth and height from the MISR CTH–OD histogram into agreement with the coarsely vertically resolved area-averaged cloud properties. That is to say, we wish to find a distribution of liquid and ice content within the bounds of the MISR CTH–OD histogram such that it satisfies the observed liquid and ice water path resolved into low, middle, and high categories and the observed effective radius of liquid and ice. This database is resolved in time and space and covers the Southern Ocean for the period 2007–08. For each month and latitude–longitude point within the database, there is a data structure that describes the clouds that occur in that month and region. Cloud scenes are categorized into several possible configurations of plane-parallel clouds, and each data structure describes the frequencies of the different cloud configurations. We will refer to these configurations as elements of the data structure. The usefulness of the creation of this database is twofold: First, it allows evaluation of the extent to which observed cloud properties are able to reproduce the observed upwelling shortwave radiation. Second, it

enables the calculation of the contributions from individual cloud properties to the upwelling shortwave radiation. In the following section, we will discuss the way in which the data structure for a given region and time in the database is created and the methodology by which an upwelling SW is calculated from it. (A flowchart describing the algorithm is provided in Fig. S1 of the supplementary material).

First, we shall describe the basic data structure used. The overarching descriptor of the cloud population is derived from the MISR CTH–OD histogram, which bins the observations for a given month and region in 16 height and 7 optical depth bins (Marchand et al. 2010). The MISR CTH–OD histogram is further refined with the use of the cloud overlap probabilities to yield four histograms similar to the original MISR CTH–OD histogram, each of which describes a particular overlap state. The four possible overlap states are as follows: none (the cloud has no clouds in other height categories beneath it), low beneath the topmost cloud, middle and low beneath the topmost cloud, and middle beneath the topmost cloud. The overlap probability and overlap cases are described in detail in section 2b. The overlap probabilities are defined in terms of the low, middle, and high categories. Because of the systematic errors present in the detection of low-altitude liquid cloud fraction by *CloudSat* (Stephens et al. 2002), we have chosen to utilize a random overlap probability in the calculation of the low cloud fraction instead of the 2B-GEOPROF overlap probability, which is used for upper-level clouds. By combining the overlap probability with the MISR cloud fraction, a cloud fraction is calculated for each element of the data structure.

The combined MISR CTH–OD histogram and cloud overlap yields a data structure that contains $16 \times 7 \times 4$ elements that correspond to combinations of cloud-top height (16), cloud optical thickness (7), and cloud overlap (4). This data structure for a given month and location is sparsely filled because some overlap cases are impossible given the cloud-top height detected by MISR or no clouds have been detected in that particular optical depth and height range. For instance, low and middle cloud beneath a high cloud may only occur in elements of the data structure that correspond to a high-topped cloud. Elements of the data structure that have a nonzero cloud fraction contain the cloud properties and the atmospheric sounding data that the radiative transfer algorithm requires to calculate an upwelling flux of shortwave radiation.

The clouds described by the data structure must be consistent with the input data from observations. These input data are as follows: the near-cloud-top liquid effective radius as measured by MODIS; the ice effective radius and the IWP as retrieved by the 2C-ICE algorithm; the liquid water path from UWISC partitioned vertically utilizing data from 2B-CWC-RO (UWISC+2B-CWC-RO); the CTH–OD histogram from MISR; and the overlap probability measured by 2B-GEOPROF. For instance, the observed overall liquid water path from UWISC+2B-CWC-RO for a given time and location should be the same as the liquid water path calculated using all the elements of the data structure. Monthly average data were used for all observations so that the combination of the aforementioned datasets was not dependent on sampling the same clouds on each satellite overpass.

We will now describe the calculation of liquid and ice water contents within the elements of the data structure that are consistent with the observed coarsely resolved liquid and ice water paths as well as the effective radii of liquid and ice. In other words, we will find a distribution of liquid and ice within the granular distribution from MISR CTH–OD that satisfies the coarsely vertically resolved liquid and ice water paths and the effective radii of liquid and ice. This is accomplished by dividing the optical depth pertaining to each element of the data structure into contributions from liquid and ice as well as contributions from low, middle, and high clouds. The optical thickness that describes the cloud in a given data structure element pertaining to the optical depth range $\tilde{\tau}$, a given topmost CTP, and one of the four potential overlap cases ($\eta \in [1, 4]$) is written as $\tau_{\mathrm{CTP},\tilde{\tau},\eta}$. The optical thickness $\tau_{\mathrm{CTP},\tilde{\tau},\eta}$ exists between the bounds of the MISR optical depth histogram for $\tilde{\tau}$. We may write the optical depth for the data structure element as a sum of all contributions from categories and phases where *LMH* refers to the low, middle, and high cloud height categories that exist in the data structure element; CTP refers to the topmost cloud's cloud-top pressure; and "ice, liq" refers to the ice and liquid phases,

$$\tau_{\mathrm{CTP},\tilde{\tau},\eta} = \sum_{m}^{LMH} \sum_{p}^{\mathrm{ice,liq}} \boldsymbol{\tau}_{mp}, \tag{1}$$

where the sums are over the existing categories and phases within the atmospheric column that describes the clouds which exist in a given element of the data structure.

We may write the 3×2 matrix of contributions to the optical thickness $\boldsymbol{\tau}_{mp}$ as the product of the scalar total optical thickness $\tau_{\mathrm{CTP},\tilde{\tau},\eta}$ for a given data structure element with a 3×2 coefficient matrix $\mathbf{C}$,

$$\mathbf{C}\tau_{\mathrm{CTP},\tilde{\tau},\eta} = \boldsymbol{\tau}_{mp}, \tag{2}$$

where the matrix $\boldsymbol{\tau}_{mp}$ that will be used to calculate water paths is written as

$$\boldsymbol{\tau}_{mp} = \begin{pmatrix} \tau_{H,\text{ice}} & \tau_{H,\text{liq}} \\ \tau_{M,\text{ice}} & \tau_{M,\text{liq}} \\ \tau_{L,\text{ice}} & \tau_{L,\text{liq}} \end{pmatrix} \tag{3}$$

and where $\mathbf{C}$ is the matrix

$$\mathbf{C} = \begin{pmatrix} a_H b_{H,\text{ice}} & a_H b_{H,\text{liq}} \\ a_M b_{M,\text{ice}} & a_M b_{M,\text{liq}} \\ a_L b_{L,\text{ice}} & a_L b_{L,\text{liq}} \end{pmatrix}, \tag{4}$$

that contains the coefficients a_m, which apportion the optical thickness vertically between low, middle, and high categories, and coefficients $b_{m,p}$, which apportion the optical thickness of a given layer between liquid and ice (liq,ice). The coefficients are defined such that $\tau_{\text{CTP},\tilde{\tau},\eta}$ for a given data structure element is completely accounted for by the sum of clouds in the three height categories and two phases such that

$$\sum_{m}^{LMH} a_m = 1 \quad \text{and} \quad \sum_{p}^{\text{ice,liq}} b_{m,p} = 1. \tag{5}$$

To calculate water paths for an element of the data structure we must know a_m, $b_{m,p}$, and $\tau_{\text{CTP},\tilde{\tau},\eta}$. The value of $b_{m,p}$ for the data structure at a given time and location is determined by assuming that in each height category the ratio of ice to liquid does not depend on the overlying clouds height or the optical depth of the clouds in the column and only depends on the coarse cloud category. This means that the clouds in a given height category all have the same ratio of ice to liquid. Thus, we may calculate $b_{m,p}$ for all CTP, $\tilde{\tau}$, η in a given data structure in the database using the liquid and ice water paths contained in UWISC+2B-CWC-RO and 2C-ICE for each category and the appropriate effective radii from MODIS and 2C-ICE that correspond to the location and time of the data structure. The low, middle, and high cloud categories are each assigned an average ice effective radius derived from the 2C-ICE dataset and all liquid clouds are assigned a liquid effective radius consistent with MODIS.

This leaves $\tau_{\text{CTP},\tilde{\tau},\eta}$ and a_m as unknowns. We do not know which value of $\tau_{\text{CTP},\tilde{\tau},\eta}$ between the bounds of the MISR histogram optical depth intervals best describes the clouds within that element of the data structure. The MISR histogram bins are set to be consistent with ISCCP bins and are quite wide; thus, the choice of a mean bin optical thickness is important. The mean optical thickness within a histogram bin is observable, but the objective here is to compute reflected shortwave radiation from observed intrinsic cloud properties and to evaluate the sensitivity of $\text{SW}^{\uparrow}$ to variation in these cloud properties rather than calculate $\text{SW}^{\uparrow}$ from τ. In addition, there is no way to determine the values of a_m observationally. There are many configurations of the values of $a_m(\text{CTP}, \tilde{\tau}, \eta)$ and $\tau_{\text{CTP},\tilde{\tau},\eta}$ constrained by the bin edges of the MISR CTH–OD histogram within the data structure that satisfy the observed liquid water path, ice water path, cloud fraction, and effective radius for the data structure as a whole, and we wish to select one of these in a way which does not assign an a priori distribution of optical thickness.

To objectively choose a configuration of $\tau_{\text{CTP},\tilde{\tau},\eta}$ and $a_m(\text{CTP}, \tilde{\tau}, \eta)$ across the data structure that satisfies the observational constraints for that location and time, we utilize a Monte Carlo technique similar to Kirkpatrick et al. (1983). The Monte Carlo is used to determine values of $a_m(\text{CTP}, \tilde{\tau}, \eta)$ and $\tau_{\text{CTP},\tilde{\tau},\eta}$ that minimize the difference $\tilde{\Delta}\text{WP}$ between observed and modeled area-averaged water paths (WP and WP′, respectively) for ice and liquid and each height category, as given by

$$\tilde{\Delta}\text{WP} = \sqrt{\sum_{m}^{LMH} \sum_{p}^{\text{ice,liq}} (\text{WP}_{m,p} - \text{WP}'_{m,p})^2}. \tag{6}$$

The area-averaged water path in each category and phase $\text{WP}'_{m,p}$ is calculated using the liquid and ice water path and cloud fraction contained in the data structure. In the creation of water paths within the data structure, the liquid and ice water path for a given $\boldsymbol{\tau}_{m,p}$ are calculated using the observed cloud-top effective radius of liquid and the effective radius of ice for that category. Coefficients from Heymsfield et al. (2003) are used in the calculation of IWP from the optical depth and effective radius of ice. Liquid water path as a function of r_e and τ is calculated according to Slingo (1989). We have chosen to use a Monte Carlo as described above because it does not assume a priori a distribution of mean optical depths within the elements of the MISR CTH–OD histogram or the distribution of optical depth between coarse vertical levels, and it only requires that the data structure generated by this method conforms to all the observed cloud properties for that region and time.

Using the method described above, the distribution of ice and liquid is found that is determined by the Monte Carlo algorithm to be in agreement with observations from 2C-ICE and UWISC+2B-CWC-RO; the observed effective radii of ice and liquid; and the bin edges of MISR and the cloud fraction distribution within the MISR histogram. Any residual difference between the observed liquid and ice water path in each layer and the values calculated from the data structure are removed by multiplying the water path in each height category, phase, and element of the data structure by

a constant factor equal to the ratio of observed to modeled water paths in that height category and phase for that element of the database. This process is used to create a database of mean monthly cloud populations over the Southern Ocean for 1.18° × 12° (latitude × longitude) regions during the period 2007–08.

From the data structure for a given region and time we may calculate upwelling shortwave radiation utilizing the Rapid Radiative Transfer Algorithm for GCMs (RRTMG) (Mlawer et al. 1997) and the surface albedo parameterization of Jin et al. (2011). Calculations were performed using a modified version of RRTMG with liquid cloud optical properties from Mie calculations using a modified gamma size distribution with dispersion equal to 0.12. These properties are planned to be implemented in a future version of RRTMG (E. J. Mlawer 2013, personal communication).

To calculate the monthly-mean upwelling shortwave flux from our data structure, orbital equations were used to calculate the distribution of θ_0 for a given month and location. The $SW^{\uparrow}$ for each element of the data structure was calculated for six evenly spaced θ_0 values within the month's range. These values were then interpolated to 150 values of θ_0. Values of $SW^{\uparrow}$ at each interpolated θ_0 were weighted by time and cloud fraction for each data structure element to calculate a monthly-mean $SW^{\uparrow}$ for a given region.

For each cloud layer represented within each element of the data structure the RRTMG was supplied with a vertically homogeneous layer consisting of liquid and ice of fixed pressure thickness consistent with Wang et al. (2000). A single mean effective radius is provided for the liquid, and a single mean effective radius is provided for the ice. MODIS retrieves droplet effective radius close to cloud top (Platnick 2000). To calculate an r_e that describes the r_e throughout the cloud rather than just near cloud top it is assumed that LWC increases linearly with height from cloud base that, at least for low clouds, is consistent with observations (Painemal and Zuidema 2011). Thus, using the method described by Brenguier et al. (2000), we calculate an effective radius for a vertically homogeneous layer that has the same LWP and optical depth as observed. This equates to an r_e value that is 5/6 of the retrieved cloud-top r_e and thus results in a higher reflectance. We also show comparisons to observations at the end of this section using the unmodified retrieved r_e to give some indication of the uncertainty range introduced by these assumptions.

To test the realism of our cloud database and the accuracy of our radiative transfer calculations we compared our calculated monthly $SW^{\uparrow}$ values to those from CERES Energy Balanced and Filled (EBAF) 2.6r (Loeb et al. 2009). To examine the implications of uncertainty in observed cloud properties in the calculation of $SW^{\uparrow}$ the data used as input to the algorithm have been repeated many times varying the observed liquid water path, the ice water path, and the effective radius between the minimum and maximum of the uncertainty range attached to each dataset. (A list of different cases is shown in Tables S1 and S2 of the supplementary material online.) While the abridged list (for computational efficiency) of possible input cases studied does not completely evaluate the range in $SW^{\uparrow}$ because of input uncertainty, it does allow a rough estimation of the dependence of upwelling shortwave radiation on uncertainty in the input data.

The seasonal cycle of $SW^{\uparrow}$ and reflectivity [defined as the ratio $SW^{\uparrow}SW_{\downarrow}^{-1}$ at the top of the atmosphere (TOA)] compared to CERES is shown in Fig. 11. Comparing observed and calculated $SW^{\uparrow}$ found values of $R \geq 0.95$ and comparing observed and calculated reflectivity, which is more sensitive to small errors in wintertime shortwave flux, found values of $R \geq 0.67$ (Fig. 12). Wintertime upwelling shortwave flux tends to be lower than the CERES data by a small amount. Because of the overall low shortwave flux in the wintertime, this leads to relatively large errors in reflectivity. This issue persists in the clear sky albedo as well indicating that is may not be an issue related to cloud properties. Potential sources of disagreement between the reconstructed $SW^{\uparrow}$ and the CERES data could include failure of the plane-parallel assumption, lack of a twilight irradiance (Kato and Loeb 2003) in the reconstructed $SW^{\uparrow}$, and uncertainty in the surface albedo parameterization. Despite these potential sources of error, the variable of interest in simulating Earth's energy balance, the shortwave flux, agrees well overall.

Grosvenor et al. (2012) and Chubb et al. (2013) reported that in situ observations of Southern Hemisphere high-latitude low clouds from aircraft show high abundances of supercooled water but relatively infrequent observations of ice particles. Chubb et al. (2013) also noted the frequent occurrence of drizzle, which, because of the large size of drizzle drops, may be confused with ice by the active remote sensing instruments. In consideration of this possible systematic error in the 2C-ICE data, we also show the case in which low cloud ice is set to be zero and no additional liquid water is created (Figs. 11 and 12). Removal of the low cloud ice reduces the Southern Ocean reflectivity, especially during the winter. However, because of the relatively weak radiative effect of ice, the reduction in $SW^{\uparrow}$ is not large relative to the uncertainty in the other cloud properties, such as the MODIS channel used to retrieve r_e or its assumed profile within the cloud. This is demonstrated in Figs. 11 and 12 by the large spread of the cases that

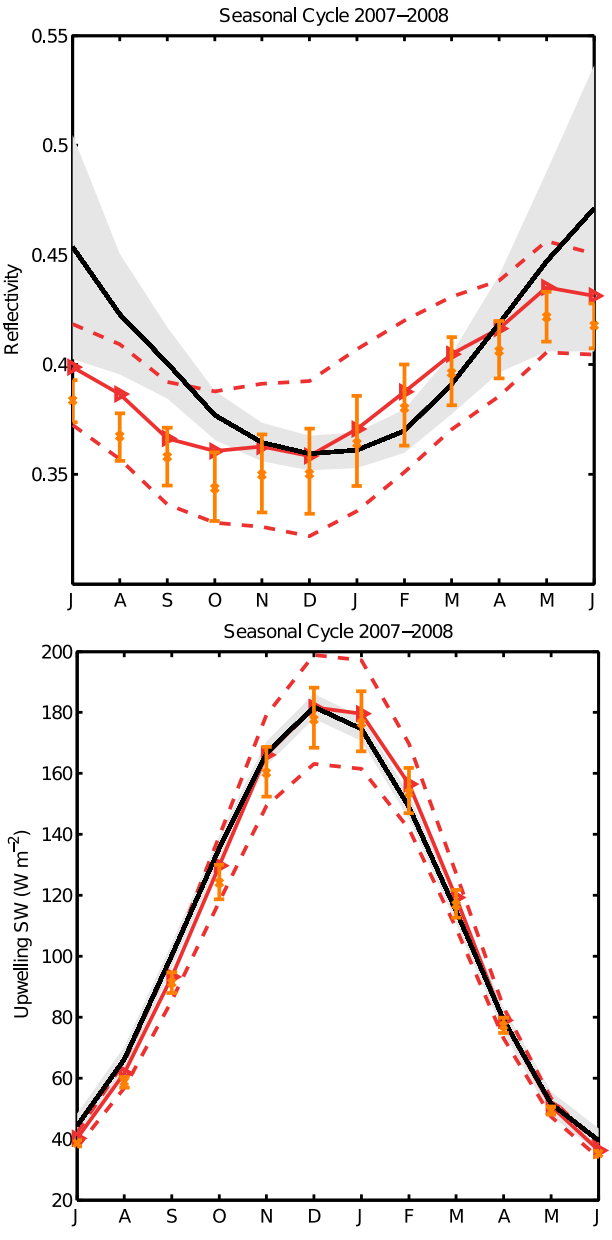

FIG. 11. Comparison of $SW^{\uparrow}$ between CERES EBAF 2.6r observations and calculations from the remotely sensed data using RRTMG. Comparisons are shown with (top) reflectivity and (bottom) upwelling shortwave radiation. All comparisons are over oceans between 40° and 60°S. Black lines give the mean value of the CERES data, and gray lines show its uncertainty range. Red lines show the results calculated by RRTMG from an ensemble where each ensemble member is created by setting input data to the minimum and maximum of the uncertainty for that dataset. Red triangles show the mean over the ensemble members, and red dashed lines show the maximum and minimum of the ensemble members. Orange shows the results of six cases that were created by setting the low cloud ice to zero. The six cases with no low cloud ice were created using r_e generated by the combination of the three MODIS r_e retrieval bands and the two assumed vertical profiles of r_e that are discussed in the text. Orange crosses show the mean of these cases, and orange error bars show the minimum and maximum over these cases.

have no low-altitude ice. While it is probably somewhat unphysical that no ice exists at pressures above 680 hPa, it is also worthwhile to consider the results from the 2C-ICE carefully given that the radiative signature of the low cloud ice is negligible.

4. The impact of cloud properties on TOA CRE

Because the upwelling shortwave radiation computed from our synthesis of remotely detected cloud properties is in agreement with observations of upwelling shortwave radiation, this analysis framework may be used to probe the importance of variability in individual cloud properties for the $SW^{\uparrow}$ over the Southern Ocean. The framework of this analysis makes it relatively straightforward to alter cloud properties and recompute the upwelling shortwave radiation, thus allowing examination of the contributions of annual variation in cloud properties to the annual variation in albedo.

The effect of the annual cycle of various cloud properties on the upwelling shortwave radiation is examined because the annual cycle is the strongest signal in most cloud properties. To examine the impact of the seasonal cycle of a given cloud property on shortwave flux, $SW^{\uparrow}$ is recomputed using the annual-mean distribution of that property contained in each data structure, while allowing the distribution of the other properties to vary. The resulting distribution contained in the data structure is denoted as $\bar{\xi}$. We then define the variation in cloud radiative effect (CRE) due to variation in cloud properties as $\mathrm{CRE}(\xi) - \mathrm{CRE}(\bar{\xi})$, where ξ refers to the case where the distributions of all cloud properties are allowed to vary according to their seasonal cycles. To study the effects of the seasonal cycle of the radiatively dominant low cloud fraction the cloud fraction within each data structure is adjusted to keep the low cloud fraction constant while allowing upper-level cloud fractions to freely vary. That is to say, for a given month and location both the low cloud with no overlying cloud and the low cloud beneath overlying cloud will be adjusted.

An ensemble is created to test the uncertainty in the impact of the annual cycle of a given cloud property on changes in $SW^{\uparrow}$ because of measurement uncertainty in the observations used as input. Ensemble members are created by randomly selecting values for each input variable from values that are normally distributed about the mean observed value and within the measurement uncertainty at each point in time and space. The input variables that are selected from normal distributions within the observational uncertainty are as follows: the liquid and ice water paths; the effective radius of ice and liquid (the latter is assumed to be adiabatically distributed); the probability of cloud overlap from *CloudSat*; and the ratio

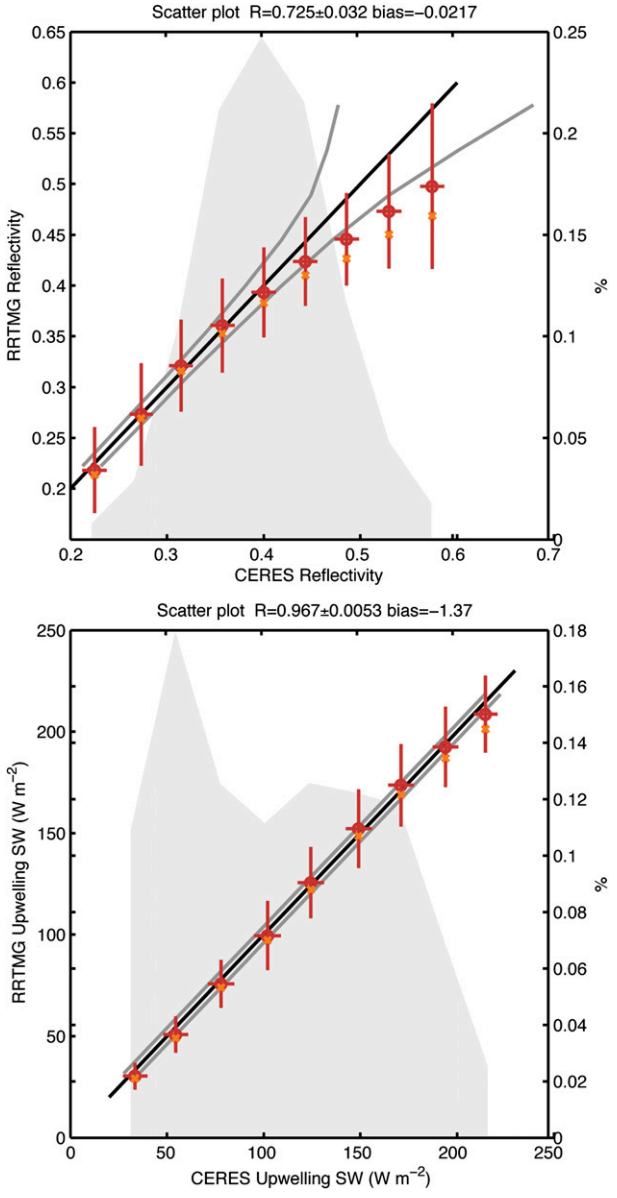

FIG. 12. Comparison of $SW^{\uparrow}$ between CERES EBAF 2.6r observations and calculations from the remotely sensed data using RRTMG (left axis) for 40°–60°S. Comparisons are shown with (top) reflectivity and (bottom) upwelling shortwave radiation. Error bars display the standard deviation for all values within a given bin. The solid black diagonal line shows the 1:1 relation. Gray lines on either side of the 1:1 line give the uncertainty bounds for the CERES data. Mean R values over ensemble members and standard deviation are shown above each panel. Also shown as gray shading is the PDF (%; right axis) of observed values in each bin. Ensemble members are created as in Fig. 11, as are the results of the case with no low cloud ice: these are shown in red and orange, respectively.

of liquid in each height category from 2C-CWC-RO. For each calculation of $\mathrm{CRE}(\xi) - \mathrm{CRE}(\bar{\xi})$, 10 ensemble members are created, and an estimate of the uncertainly of this value due to uncertainty in input variables is

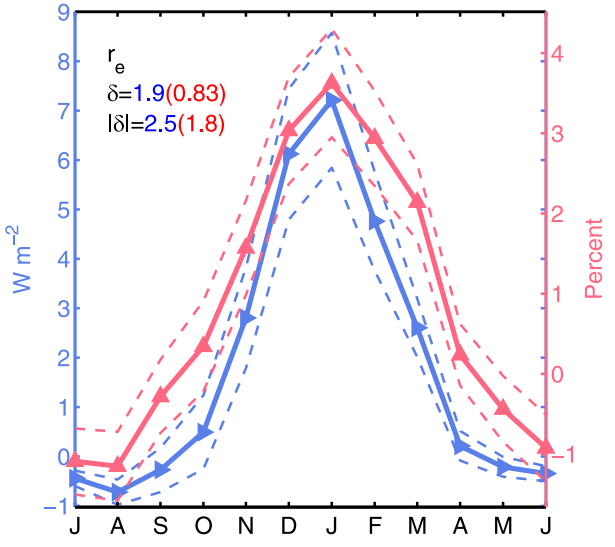

FIG. 13. Change in $SW^{\uparrow}$ [$\Delta SW^{\uparrow} = SW^{\uparrow} - SW^{\uparrow}(\overline{r_e})$] due to variation in r_e (blue) and the change in $SW^{\uparrow}$ scaled by total $SW^{\uparrow}$ (%; red). The variable δ shown in the title gives the mean impact of variations in r_e on TOA SW, and $|\delta|$ shows the mean of the absolute value of differences. Values listed in parentheses correspond to scaled values (%). Scaled values are calculated at each point and averaged over the Southern Ocean. Uncertainty is shown for each month using dashed lines and is calculated as the average of the standard deviation between ensemble members at each grid point.

calculated. We will now discuss the effect on $SW^{\uparrow}$ of each seasonal cycle calculated in this way.

The effect of the observed annual variation of r_e in low cloud shows a strong contribution to CRE between 6 and 8 W m^{-2} (or around 2%–4% of the $SW^{\uparrow}$ as calculated by dividing the change in CRE in each location and month by the unperturbed $SW^{\uparrow}$ for that location and month and taking the mean of the fractional changes for all locations) during the summer months because of the decrease in droplet size as seen in Fig. 13. There is a mean annual contribution of 1.9 W m^{-2} (0.84%) to $SW^{\uparrow}$ and an absolute contribution (e.g., the mean of the absolute values of the difference) of 2.5 W m^{-2} (1.8%). This result is intriguing as it implies that some appreciable amount of summertime cloud brightness in the Southern Ocean is due to the seasonal cycle of r_e. Providing that r_e is controlled by N_d more than LWP, this is consistent with Kruger and Grassl (2011), who found a high level of correlation between marine CCN production and liquid cloud optical depth. It is also interesting to note that this result is similar to the estimated impact of dimethyl sulfide on the coupled ECHAM5 with the Hamburg Aerosol Model (HAM) and Model for Ozone and Related Chemical Tracers (MOZART) (ECHAM5-HAMMOZ) model. Cloud fraction was found to be increased by 2.5%, r_e was found to decrease by 15%–18%, and upwelling shortwave radiation in the summer increased by 9.32 W m^{-2}

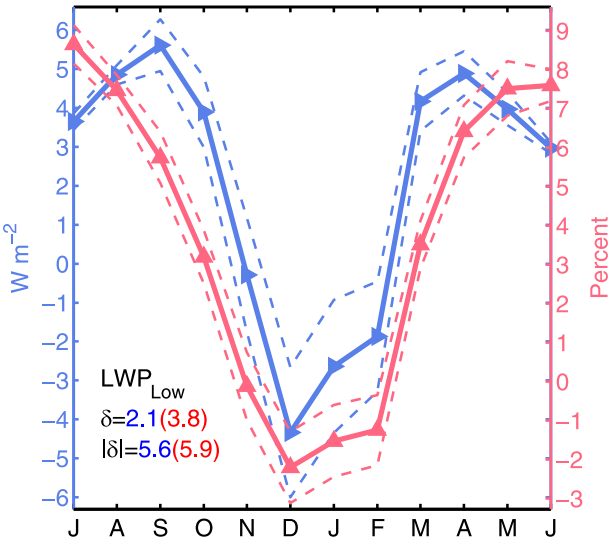

FIG. 14. As in Fig. 13, but showing the impact of variation in in-cloud LWP at pressures greater than 680 hPa [$\Delta SW^{\uparrow} = SW^{\uparrow} - SW^{\uparrow}(\overline{LWP})$].

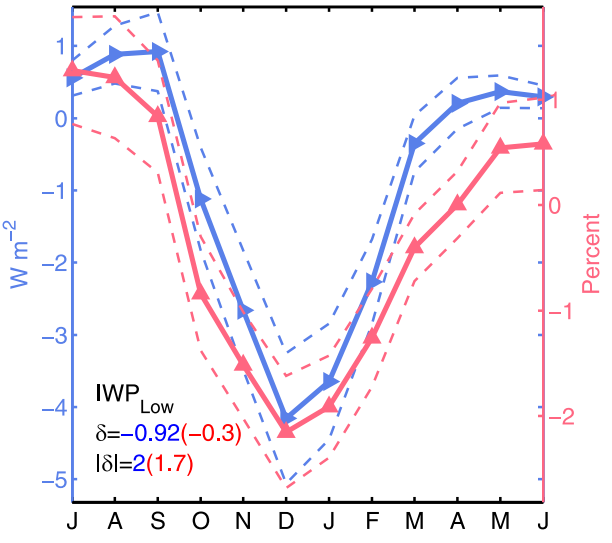

FIG. 15. As in Fig. 13, but showing the impact of variation in in-cloud IWP at pressures greater than 680 hPa [$\Delta SW^{\uparrow} = SW^{\uparrow} - SW^{\uparrow}(\overline{IWP})$].

upon the inclusion of dimethyl sulfide emissions in the model (Thomas et al. 2010).

We may also examine the effects of using the annual average in-cloud liquid water path for low clouds rather than the seasonally varying one (Fig. 14). We can see that the peaking of total water path at pressures above 680 hPa in wintertime contributes positively to the CRE during this season [3–6 W m^{-2} (5%–8%)], while the summertime decrease in in-cloud liquid water paths in the low cloud leads to a decrease in CRE [1–4 W m^{-2} (1%–3%)]. The seasonal cycle of LWP makes a mean contribution to $SW^{\uparrow}$ of 2.1 W m^{-2} (3.8%) and an absolute contribution of 5.7 W m^{-2} (6%). The fact that the wintertime $SW^{\uparrow}$ computed from these cloud properties is not significantly overestimated compared to CERES gives us some confidence in the observed wintertime increase in LWP diagnosed by MISR and UWISC because Fig. 14 suggests that without such an increase the wintertime $SW^{\uparrow}$ would be much less than observed by CERES.

Similarly to the examination of the impact of the seasonal cycle of in-cloud liquid water path within the low clouds performed above, the effect of using the average in-cloud ice water path for low clouds rather than the seasonally varying one is investigated. The seasonal cycle of in-cloud ice water path has a significant radiative impact (Fig. 15), producing a decrease in $SW^{\uparrow}$ ranging from 3 to 5 W m^{-2} (1%–2%) during the summer and an increase less than 1 W m^{-2} (<1%) during the winter. The seasonal cycle of in-cloud ice water path makes a mean contribution to $SW^{\uparrow}$ of −0.93 W m^{-2} (−0.3%) and an absolute contribution of 2 W m^{-2} (1.7%).

Given that MISR effectively detects low cloud and that they exhibit a strong annual cycle, we examine the impact of low cloud fraction variations on the $SW^{\uparrow}$. For each month we adjust the total cloud fraction in the low category to be equal to the annual-mean value. The distribution of clouds in optical depth and height is different in every month. The distribution for each month is adjusted by a constant multiple so that the total low cloud for that month is equal to the annual-mean low cloud fraction. In cases where no cloud fraction is retrieved, a spline fit is used to fill in missing values so that an annual mean may be calculated. The fractional change in CRE due to variation in low cloud coverage is shown in Fig. 16. The increase in low-level cloud in the summer increases $SW^{\uparrow}$ by approximately 9–11 W m^{-2} (2%–4%) and the decrease in low-level cloud in the winter decreases SW flux by approximately 3 W m^{-2} (6%–8%). The seasonal cycle of cloud fraction is relatively symmetric with a small mean effect on the SW radiation of 2.1 W m^{-2} (−1.5%), where the difference in sign is due to the latitudinal gradient of insolation, but a large absolute contribution of 8.3 W m^{-2} (7.7%).

Finally, we attempt to quantify the significance of the seasonal transition of ice to liquid in middle and low cloud for a fixed total water path. Figures 17 and 18 show the impact on $SW^{\uparrow}$ for two different microphysical assumptions in order to illustrate the likely importance of considering how r_e changes during phase transitions. In the first case, the extra liquid mass resulting from decreases in ice fraction is transferred to the existing number of droplets so that r_e increases. In the second case, we keep r_e the same and thus assume that the extra

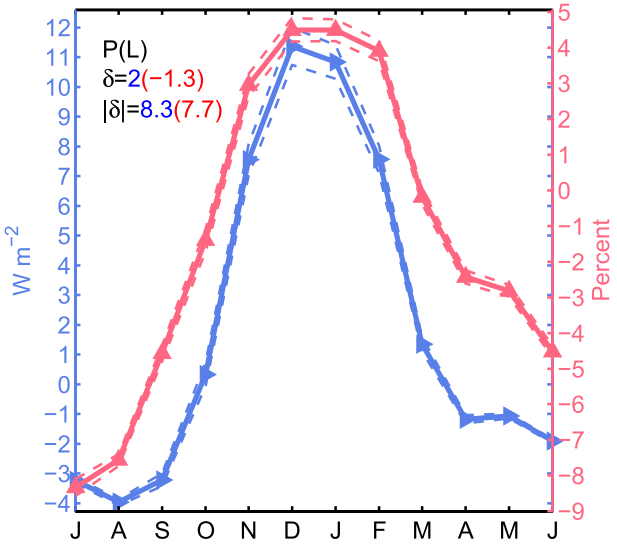

FIG. 16. As in Fig. 13, but showing the impact of variation in low cloud fraction [$\Delta SW^{\uparrow} = SW^{\uparrow} - SW^{\uparrow}(\overline{CF_L})$].

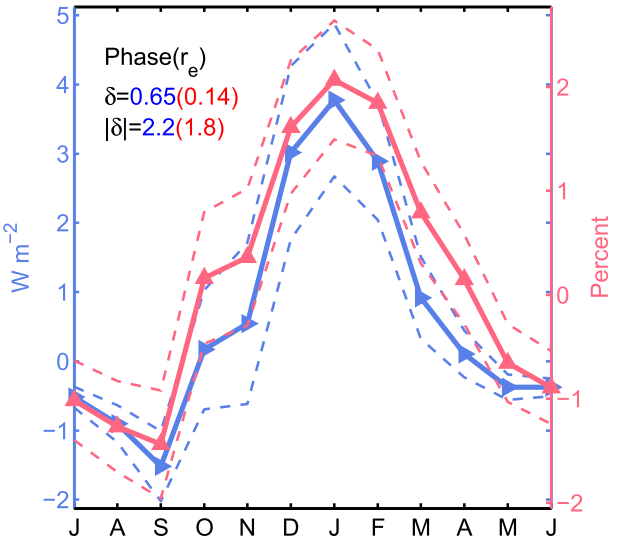

FIG. 17. As in Fig. 13, but showing the impact of variation in the ratio LWP/IWP at pressures >680 hPa [$\Delta SW^{\uparrow} = SW^{\uparrow} - SW^{\uparrow}(\overline{LWP/IWP})$]. In equalizing the ratio of liquid and ice at pressures >680 hPa, r_e is held fixed.

water mass becomes additional cloud droplets. We see that the increase in liquid fraction during the summer increases the upwelling shortwave radiation in this season. This brightening is strengthened by holding the r_e fixed rather than the number of droplets as seen by comparing Fig. 17 with Fig. 18. Summertime increases yield increases in upwelling SW around 2–4 W m^{-2} (1%–2%) in the former case and around 1–2 W m^{-2} (<1%) in the latter. The difference in the strength of the phase transition dependent on microphysical assumptions draws attention to the importance of careful consideration of the influence of cloud microphysics in the Southern Ocean region on the upwelling shortwave radiation. However, in reality the situation is likely complicated beyond the two simple cases we have presented here by feedbacks between the presence of ice, precipitation, cloud dynamics, aerosol scavenging, and cloud coverage as described by Morrison et al. (2011) and Berner et al. (2013). It is possible that in a case where CCN does not change drastically the constant r_e case might be more accurate given the occurrence of small regions of pure liquid and ice in mixed phase (Grosvenor et al. 2012; Vidaurre and Hallett 2009). These two simple cases are selected to indicate the radiative impact of the liquid to ice transition in low cloud in the Southern Ocean and demonstrate the importance of constraining the microphysics during such transitions. Our calculated changes in upwelling shortwave radiation, performed assuming non-interacting liquid and ice, are likely to be smaller than a case where ice and liquid interactions were simulated since it is likely that increases in total water path would occur with decreasing ice because of a reduction in precipitation. Because of the poorly constrained nature of the interactions between mixed-phase microphysics and macrophysics, we offer the simpler case where ice and liquid do not affect each other.

5. Summary and discussion

We have presented observational datasets detailing the annual cycles and latitudinal structure of cloud properties that affect cloud reflectivity. These datasets were combined and analyzed using a procedure designed to assimilate

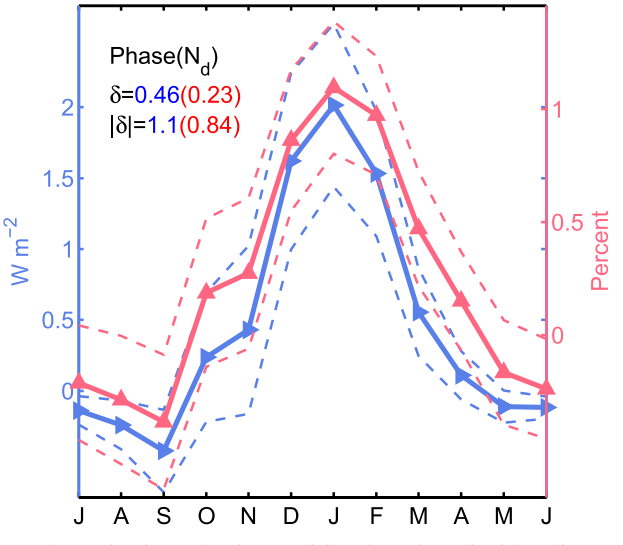

FIG. 18. As in Fig. 17, but in equalizing the ratio of liquid and ice at pressures >680 hPa, N_d is held fixed.

multiple remote sensing instruments. The upwelling shortwave radiation was calculated from this cloud property construction and the reflected radiation generated by this method was found to explain more than 92% of the variance in observations. Using the radiative transfer model, we were able to test the sensitivity of upwelling shortwave radiation to variations in cloud properties.

- Liquid effective radius at cloud top is observed to have a pronounced seasonal cycle with a lower effective radius in summer causing a significant cloud brightening. We find that setting the effective radius to the mean annual value decreases $SW^{\uparrow}$ during summer by 4–8 $W m^{-2}$ relative to $SW^{\uparrow}$ when r_e is allowed to vary seasonally.
- MISR shows a summertime peak in low cloud fraction and wintertime peaks in middle and high cloud consistent with lower-tropospheric stability and synoptic activity, respectively. These results are in agreement with several previous studies (Klein and Hartmann 1993; Wood and Bretherton 2006; Haynes et al. 2011; Bromwich et al. 2012). We find that the variations in low cloud fraction account for a percentage of shortwave CRE that is roughly proportional to the cloud coverage variation. The increase in low cloud coverage in the summer is responsible for around 9–11 $W m^{-2}$ of increased $SW^{\uparrow}$ relative to the mean. This effect, combined with the summertime brightening due to decreased r_e, as described above, indicates the importance of the simulation of both these effects in climate models to correctly reproduce the upwelling shortwave radiation in the Southern Ocean in both mean state and warmed climates. This appears to not be the case with respect to the seasonal cycle of low cloud fraction in previous generations of climate models. CMIP3 models do not effectively reproduce the observed correlation between stability and cloud fraction or an increase in cloud fraction in a warmed climate, consistent with maintaining the observed relationship of stability and cloud fraction (CF) under a robust 0.5–1-K increase in estimated inversion strength (Caldwell et al. 2013). Thus, climate models might underrepresent both the pronounced effect of low cloud changes on the seasonal cycle of $SW^{\uparrow}$ as described here and potential increases in $SW^{\uparrow}$ in a warmed climate because of increased low cloud coverage in step with strengthening inversions.
- Using microwave, radar, and lidar, we show a pronounced wintertime increase in total condensed water in low cloud. This may result from efficient longwave cooling at cloud top during the lengthy winter nights in this region (Morrison et al. 2011). The increase in wintertime in-cloud liquid and ice is supported by our calculations of the annual cycle of upwelling shortwave radiation. Without the wintertime increase in in-cloud LWP and IWP the reflected wintertime shortwave radiation that we calculate would be much less than observed. Despite a marked decrease in the summer, a large amount of ice is still found in low clouds by the 2C-ICE algorithm, which gives them the possibility of further brightening as the ice transitions to liquid in a warmed climate. On the other hand, the radiative signature of the low cloud ice was found to be relatively faint compared to the rest of the constituents of the cloud systems in the Southern Ocean, while the potential effect of the transition between liquid and ice over the course of a year was found to be pronounced. This reinforces the need for further in situ measurements of low cloud ice in the pristine Southern Ocean such as pursued by Grosvenor et al. (2012) and Chubb et al. (2013) and merged data products investigating cloud ice such as those described by Huang et al. (2006). If low cloud ice exists in the Southern Ocean to the extent that it is diagnosed by the current generation of remote sensing instruments, it has the potential of affecting the climate system. This is investigated in the second part of this paper (McCoy et al. 2014).

Acknowledgments. This research was conducted with support from NASA MAP Grant NNX09AH73G and Government support under and awarded by DoD Air Force Office of Scientific Research National Defense Science and Engineering Graduate (NDSEG) Fellowship 32 CFR 168a. The authors would also like to thank Peter Blossey and Marc Michelsen for extensive technical support; Thomas Ackerman, Chris Bretherton, Qiang Fu, John McCoy, Robert Wood, and Mark Zelinka for useful discussion and advice; and Jennifer Kay for sharing data from Kay and Gettelman (2009). CERES data were obtained from the NASA Langley Research Center CERES ordering tool (at http://ceres.larc.nasa.gov/). MODIS data were obtained from the NASA Goddard Land Processes data archive.

REFERENCES

Austin, R. T., and G. L. Stephens, 2001: Retrieval of stratus cloud microphysical parameters using millimeter-wave radar and visible optical depth in preparation for CloudSat: 1. Algorithm formulation. *J. Geophys. Res.,* **106,** 28 233–28 242, doi:10.1029/2000JD000293.

Bennartz, R., 2007: Global assessment of marine boundary layer cloud droplet number concentration from satellite. *J. Geophys. Res.,* **112,** D02201, doi:10.1029/2006JD007547.

Berner, A. H., C. S. Bretherton, R. Wood, and A. Muhlbauer, 2013: Marine boundary layer cloud regimes and POC formation in a CRM coupled to a bulk aerosol scheme. *Atmos. Chem. Phys.,* **13,** 12 549–12 572, doi:10.5194/acp-13-12549-2013.

Bony, S., and Coauthors, 2006: How well do we understand and evaluate climate change feedback processes? *J. Climate,* **19,** 3445–3482, doi:10.1175/JCLI3819.1.

Brenguier, J. L., H. Pawlowska, L. Schuller, R. Preusker, J. Fischer, and Y. Fouquart, 2000: Radiative properties of boundary layer clouds: Droplet effective radius versus number concentration. *J. Atmos. Sci.,* **57,** 803–821, doi:10.1175/1520-0469(2000)057<0803:RPOBLC>2.0.CO;2.

Breon, F. M., and M. Doutriaux-Boucher, 2005: A comparison of cloud droplet radii measured from space. *IEEE Trans. Geosci. Remote Sens.,* **43,** 1796–1805, doi:10.1109/TGRS.2005.852838.

Bromwich, D. H., and Coauthors, 2012: Tropospheric clouds in Antarctica. *Rev. Geophys.,* **50,** RG1004, doi:10.1029/2011RG000363.

Caldwell, P. M., Y. Y. Zhang, and S. A. Klein, 2013: CMIP3 subtropical stratocumulus cloud feedback interpreted through a mixed-layer model. *J. Climate,* **26,** 1607–1625, doi:10.1175/JCLI-D-12-00188.1.

Chen, R. Y., R. Wood, Z. Q. Li, R. Ferraro, and F. L. Chang, 2008: Studying the vertical variation of cloud droplet effective radius using ship and space-borne remote sensing data. *J. Geophys. Res.,* **113,** D00A02, doi:10.1029/2007JD009596.

Chepfer, H., S. Bony, D. Winker, G. Cesana, J. L. Dufresne, P. Minnis, C. J. Stubenrauch, and S. Zeng, 2009: The GCM-Oriented CALIPSO Cloud Product (CALIPSO-GOCCP). *J. Geophys. Res.,* **115,** D00H16, doi:10.1029/2009JD012251.

Chubb, T. H., J. B. Jensen, S. T. Siems, and M. J. Manton, 2013: In situ observations of supercooled liquid clouds over the Southern Ocean during the HIAPER pole-to-pole observation campaigns. *Geophys. Res. Lett.,* **40,** 5280–5285, doi:10.1002/grl.50986.

Curry, J. A., 1986: Interactions among turbulence, radiation and microphysics in Arctic stratus clouds. *J. Atmos. Sci.,* **43,** 90–106, doi:10.1175/1520-0469(1986)043<0090:IATRAM>2.0.CO;2.

Deng, M., G. G. Mace, Z. E. Wang, and H. Okamoto, 2010: Tropical Composition, Cloud and Climate Coupling Experiment validation for cirrus cloud profiling retrieval using CloudSat radar and CALIPSO lidar. *J. Geophys. Res.,* **115,** D00J15, doi:10.1029/2009JD013104.

Evan, A. T., A. K. Heidinger, and D. J. Vimont, 2007: Arguments against a physical long-term trend in global ISCCP cloud amounts. *Geophys. Res. Lett.,* **34,** L04701, doi:10.1029/2006GL028083.

Foot, J. S., 1988: Some observations of the optical-properties of clouds. I: Stratocumulus. *Quart. J. Roy. Meteor. Soc.,* **114,** 129–144, doi:10.1002/qj.49711447907.

Grosvenor, D. P., and R. Wood, 2014: The effect of solar zenith angle on MODIS cloud optical and microphysical retrievals within marine liquid water clouds. *Atmos. Chem. Phys.,* **14,** 7291–7321, doi:10.5194/acp-14-7291-2014.

——, T. W. Choularton, T. Lachlan-Cope, M. W. Gallagher, J. Crosier, K. N. Bower, R. S. Ladkin, and J. R. Dorsey, 2012: In-situ aircraft observations of ice concentrations within clouds over the Antarctic Peninsula and Larsen Ice Shelf. *Atmos. Chem. Phys.,* **12,** 11 275–11 294, doi:10.5194/acp-12-11275-2012.

Haynes, J. M., C. Jakob, W. B. Rossow, G. Tselioudis, and J. Brown, 2011: Major characteristics of Southern Ocean cloud regimes and their effects on the energy budget. *J. Climate,* **24,** 5061–5080, doi:10.1175/2011JCLI4052.1.

Heymsfield, A. J., S. Matrosov, and B. Baum, 2003: Ice water path–optical depth relationships for cirrus and deep stratiform ice cloud layers. *J. Appl. Meteor.,* **42,** 1369–1390, doi:10.1175/1520-0450(2003)042<1369:IWPDRF>2.0.CO;2.

——, and Coauthors, 2008: Testing IWC retrieval methods using radar and ancillary measurements with in situ data. *J. Appl. Meteor. Climatol.,* **47,** 135–163, doi:10.1175/2007JAMC1606.1.

Horvath, A., and R. Davies, 2007: Comparison of microwave and optical cloud water path estimates from TMI, MODIS, and MISR. *J. Geophys. Res.,* **112,** D01202, doi:10.1029/2006JD007101.

Huang, J., P. Minnis, B. Lin, Y. Yi, T.-F. Fan, S. Sun-Mack, and J. K. Ayers, 2006: Determination of ice water path in ice-over-water cloud systems using combined MODIS and AMSR-E measurements. *Geophys. Res. Lett.,* **33,** L21801, doi:10.1029/2006GL027038.

Huang, Y., S. T. Siems, M. J. Manton, L. B. Hande, and J. M. Haynes, 2012: The structure of low-altitude clouds over the Southern Ocean as seen by *CloudSat*. *J. Climate,* **25,** 2535–2546, doi:10.1175/JCLI-D-11-00131.1.

Jin, Z. H., Y. L. Qiao, Y. J. Wang, Y. H. Fang, and W. N. Yi, 2011: A new parameterization of spectral and broadband ocean surface albedo. *Opt. Express,* **19,** 26 429–26 443, doi:10.1364/OE.19.026429.

Kato, S., and N. G. Loeb, 2003: Twilight irradiance reflected by the earth estimated from Clouds and the Earth's Radiant Energy System (CERES) measurements. *J. Climate,* **16,** 2646–2650, doi:10.1175/1520-0442(2003)016<2646:TIRBTE>2.0.CO;2.

Kay, J. E., and A. Gettelman, 2009: Cloud influence on and response to seasonal Arctic sea ice loss. *J. Geophys. Res.,* **114,** D18204, doi:10.1029/2009JD011773.

King, M. D., S.-C. Tsay, S. E. Platnick, M. Wang, and K.-N. Liou, 1997: Cloud retrieval algorithms for MODIS: Optical thickness, effective particle radius, and thermodynamic phase. NASA MODIS Algorithm Theoretical Basis Doc. ATBD-MOD-05, 83 pp.

King, N. J., and G. Vaughan, 2012: Using passive remote sensing to retrieve the vertical variation of cloud droplet size in marine stratocumulus: An assessment of information content and the potential for improved retrievals from hyperspectral measurements. *J. Geophys. Res.,* **117,** D15206, doi:10.1029/2012JD017896.

——, K. N. Bower, J. Crosier, and I. Crawford, 2013: Evaluating MODIS cloud retrievals with in situ observations from VOCALS-REx. *Atmos. Chem. Phys.,* **13,** 191–209, doi:10.5194/acp-13-191-2013.

Kirkpatrick, S., C. D. Gelatt, and M. P. Vecchi, 1983: Optimization by simulated annealing. *Science,* **220,** 671–680, doi:10.1126/science.220.4598.671.

Klein, S. A., and D. L. Hartmann, 1993: The seasonal cycle of low stratiform clouds. *J. Climate,* **6,** 1587–1606, doi:10.1175/1520-0442(1993)006<1587:TSCOLS>2.0.CO;2.

Korhonen, H., K. S. Carslaw, D. V. Spracklen, G. W. Mann, and M. T. Woodhouse, 2008: Influence of oceanic dimethyl sulfide emissions on cloud condensation nuclei concentrations and seasonality over the remote Southern Hemisphere oceans: A global model study. *J. Geophys. Res.,* **113,** D15204, doi:10.1029/2007JD009718.

Kruger, O., and H. Grassl, 2011: Southern Ocean phytoplankton increases cloud albedo and reduces precipitation. *Geophys. Res. Lett.,* **38,** L08809, doi:10.1029/2011GL047116.

Loeb, N. G., and R. Davies, 1996: Observational evidence of plane parallel model biases: Apparent dependence of cloud optical depth on solar zenith angle. *J. Geophys. Res.,* **101,** 1621–1634, doi:10.1029/95JD03298.

——, and ——, 1997: Angular dependence of observed reflectances: A comparison with plane parallel theory. *J. Geophys. Res.,* **102,** 6865–6881, doi:10.1029/96JD03586.

——, and J. A. Coakley Jr., 1998: Inference of marine stratus cloud optical depths from satellite measurements: Does 1D theory apply? *J. Climate,* **11,** 215–233, doi:10.1175/1520-0442(1998)011<0215:IOMSCO>2.0.CO;2.

——, T. Varnai, and R. Davies, 1997: Effect of cloud inhomogeneities on the solar zenith angle dependence of nadir reflectance. *J. Geophys. Res.,* **102,** 9387–9395, doi:10.1029/96JD03719.

——, B. A. Wielicki, D. R. Doelling, G. L. Smith, D. F. Keyes, S. Kato, N. Manalo-Smith, and T. Wong, 2009: Toward optimal closure of the earth's top-of-atmosphere radiation budget. *J. Climate,* **22,** 748–766, doi:10.1175/2008JCLI2637.1.

Mace, G. G., 2007: Level 2 GEOPROF product process description and interface control document algorithm version 5.3. NASA Jet Propulsion Laboratory Rep., 42 pp.

——, Q. Q. Zhang, M. Vaughan, R. Marchand, G. Stephens, C. Trepte, and D. Winker, 2009: A description of hydrometeor layer occurrence statistics derived from the first year of merged Cloudsat and CALIPSO data. *J. Geophys. Res.,* **114,** D00A26, doi:10.1029/2007JD00975.

Mace, M., and M. Deng, 2011: Level 2 *CloudSat-CALIPSO* combined ice cloud property retrieval product process description document. NASA CloudSat Project Rep., 43 pp.

Marchand, R. T., T. P. Ackerman, and C. Moroney, 2007: An assessment of Multiangle Imaging Spectroradiometer (MISR) stereo-derived cloud top heights and cloud top winds using ground-based radar, lidar, and microwave radiometers. *J. Geophys. Res.,* **112,** D06204, doi:10.1029/2006JD007091.

——, ——, M. Smyth, and W. B. Rossow, 2010: A review of cloud top height and optical depth histograms from MISR, ISCCP, and MODIS. *J. Geophys. Res.,* **115,** D16206, doi:10.1029/2009JD013422.

McCoy, D. T., D. L. Hartmann, and D. P. Grosvenor, 2014: Observed Southern Ocean cloud properties and shortwave reflection. Part II: Phase changes and low cloud feedback. *J. Climate,* **27,** 8858–8868, doi:10.1175/JCLI-D-14-00288.1.

Mlawer, E. J., S. J. Taubman, P. D. Brown, M. J. Iacono, and S. A. Clough, 1997: Radiative transfer for inhomogeneous atmospheres: RRTM, a validated correlated-k model for the longwave. *J. Geophys. Res.,* **102,** 16 663–16 682, doi:10.1029/97JD00237.

Morrison, H., G. de Boer, G. Feingold, J. Harrington, M. D. Shupe, and K. Sulia, 2011: Resilience of persistent Arctic mixed-phase clouds. *Nat. Geosci.,* **5,** 11–17, doi:10.1038/ngeo1332.

Nakajima, T., and M. D. King, 1990: Determination of the optical thickness and effective particle radius of clouds from reflected solar radiation measurements. Part I: Theory. *J. Atmos. Sci.,* **47,** 1878–1893, doi:10.1175/1520-0469(1990)047<1878:DOTOTA>2.0.CO;2.

O'Dell, C. W., F. J. Wentz, and R. Bennartz, 2008: Cloud liquid water path from satellite-based passive microwave observations: A new climatology over the global oceans. *J. Climate,* **21,** 1721–1739, doi:10.1175/2007JCLI1958.1.

Painemal, D., and P. Zuidema, 2011: Assessment of MODIS cloud effective radius and optical thickness retrievals over the southeast Pacific with VOCALS-REx in situ measurements. *J. Geophys. Res.,* **116,** D24206, doi:10.1029/2011JD016155.

——, P. Minnis, and S. Sun-Mack, 2013: The impact of horizontal heterogeneities, cloud fraction, and liquid water path on warm cloud effective radii from CERES-like Aqua MODIS retrievals. *Atmos. Chem. Phys.,* **13,** 9997–10 003, doi:10.5194/acp-13-9997-2013.

Platnick, S., 2000: Vertical photon transport in cloud remote sensing problems. *J. Geophys. Res.,* **105,** 22 919–22 935, doi:10.1029/2000JD900333.

——, M. D. King, S. A. Ackerman, W. P. Menzel, B. A. Baum, J. C. Riedi, and R. A. Frey, 2003: The MODIS cloud products: Algorithms and examples from Terra. *IEEE Trans. Geosci. Remote Sens.,* **41,** 459–473, doi:10.1109/TGRS.2002.808301.

Simmonds, I., K. Keay, and E.-P. Lim, 2003: Synoptic activity in the seas around Antarctica. *Mon. Wea. Rev.,* **131,** 272–288, doi:10.1175/1520-0493(2003)131<0272:SAITSA>2.0.CO;2.

Slingo, A., 1989: A GCM parameterization for the shortwave radiative properties of water clouds. *J. Atmos. Sci.,* **46,** 1419–1427, doi:10.1175/1520-0469(1989)046<1419:AGPFTS>2.0.CO;2.

Slingo, J. M., 1980: A cloud parametrization scheme derived from GATE data for use with a numerical model. *Quart. J. Roy. Meteor. Soc.,* **106,** 747–770, doi:10.1002/qj.49710645008.

Solomon, A., M. D. Shupe, P. O. G. Persson, and H. Morrison, 2011: Moisture and dynamical interactions maintaining decoupled Arctic mixed-phase stratocumulus in the presence of a humidity inversion. *Atmos. Chem. Phys.,* **11,** 10 127–10 148, doi:10.5194/acp-11-10127-2011.

Stein, T. H. M., J. Delanoe, and R. J. Hogan, 2011: A comparison among four different retrieval methods for ice-cloud properties using data from *CloudSat, CALIPSO,* and MODIS. *J. Appl. Meteor. Climatol.,* **50,** 1952–1969, doi:10.1175/2011JAMC2646.1.

Stephens, G. L., and Coauthors, 2002: The *CloudSat* mission and the A-Train: A new dimension of space-based observations of clouds and precipitation. *Bull. Amer. Meteor. Soc.,* **83,** 1771–1790, doi:10.1175/BAMS-83-12-1771.

Thomas, M. A., P. Suntharalingam, L. Pozzoli, S. Rast, A. Devasthale, S. Kloster, J. Feichter, and T. M. Lenton, 2010: Quantification of DMS aerosol-cloud-climate interactions using ECHAM5-HAMMOZ model in current climate scenario. *Atmos. Chem. Phys.,* **10,** 7425–7438, doi:10.5194/acp-10-7425-2010.

Vallina, S. M., R. Simó, and S. Gassó, 2006: What controls CCN seasonality in the Southern Ocean? A statistical analysis based on satellite-derived chlorophyll and CCN and model-estimated OH radical and rainfall. *Global Biogeochem. Cycles,* **20,** GB1014, doi:10.1029/2005GB002597.

Verlinden, K. L., D. W. J. Thompson, and G. L. Stephens, 2011: The three-dimensional distribution of clouds over the Southern Hemisphere high latitudes. *J. Climate,* **24,** 5799–5811, doi:10.1175/2011JCLI3922.1.

Vidaurre, G., and J. Hallett, 2009: Ice and water content of stratiform mixed-phase cloud. *Quart. J. Roy. Meteor. Soc.,* **135,** 1292–1306, doi:10.1002/qj.440.

Wang, J. H., W. B. Rossow, and Y. C. Zhang, 2000: Cloud vertical structure and its variations from a 20-yr global rawinsonde dataset. *J. Climate,* **13,** 3041–3056, doi:10.1175/1520-0442(2000)013<3041:CVSAIV>2.0.CO;2.

Wood, R., and C. S. Bretherton, 2006: On the relationship between stratiform low cloud cover and lower-tropospheric stability. *J. Climate,* **19,** 6425–6432, doi:10.1175/JCLI3988.1.

——, and D. Hartmann, 2006: Spatial variability of liquid water path in marine low cloud: The importance of mesoscale cellular convection. *J. Climate,* **19,** 1748–1764, doi:10.1175/JCLI3702.1.

Wu, D. L., and Coauthors, 2009: Vertical distributions and relationships of cloud occurrence frequency as observed by MISR, AIRS, MODIS, OMI, CALIPSO, and CloudSat. *Geophys. Res. Lett.,* **36,** L09821, doi:10.1029/2009GL037464.

Zelinka, M. D., S. A. Klein, and D. L. Hartmann, 2012: Computing and partitioning cloud feedbacks using cloud property histograms. Part II: Attribution to changes in cloud amount, altitude, and optical depth. *J. Climate,* **25,** 3736–3754, doi:10.1175/JCLI-D-11-00249.1.

——, ——, K. E. Taylor, T. Andrews, M. J. Webb, J. M. Gregory, and P. M. Forster, 2013: Contributions of different cloud types to feedbacks and rapid adjustments in CMIP5. *J. Climate,* **26,** 5007–5027, doi:10.1175/JCLI-D-12-00555.1.

Zhang, Z., 2013: On the sensitivity of cloud effective radius retrieval based on spectral method to bi-modal droplet size distribution: A semi-analytical model. *J. Quant. Spectrosc. Radiat. Transfer,* **129,** 79–88, doi:10.1016/j.jqsrt.2013.05.033.

——, and S. Platnick, 2011: An assessment of differences between cloud effective particle radius retrievals for marine water clouds from three MODIS spectral bands. *J. Geophys. Res.,* **116,** D20215, doi:10.1029/2011JD016216.

——, A. S. Ackerman, G. Feingold, S. Platnick, R. Pincus, and H. Xue, 2012: Effects of cloud horizontal inhomogeneity and drizzle on remote sensing of cloud droplet effective radius: Case studies based on large-eddy simulations. *J. Geophys. Res.,* **117,** D19208, doi:10.1029/2012JD017655.

Zinner, T., G. Wind, S. Platnick, and A. S. Ackerman, 2010: Testing remote sensing on artificial observations: Impact of drizzle and 3-D cloud structure on effective radius retrievals. *Atmos. Chem. Phys.,* **10,** 9535–9549, doi:10.5194/acp-10-9535-2010.